

Subject Areas:

Natural Convection, Turbulence

Keywords:

Rayleigh-Bénard Convection, Non-Oberbeck-Boussinesq conditions, Low-Mach-number equations, Direct Numerical Simulation, Large-Eddy Simulation

Author for correspondence:

William A. Hay

e-mail: william.hay@uclouvain.be

Numerical simulations of turbulent thermal convection with a free-slip upper boundary

W. A. Hay and M. V. Papalexandris

Université catholique de Louvain, Institute of Mechanics, Materials and Civil Engineering, B-1348 Louvain-la-Neuve, Belgium

In this paper we report on direct numerical and large-eddy simulations of turbulent thermal convection without invoking the Oberbeck-Boussinesq approximation. The working medium is liquid water and we employ a free-slip upper boundary condition. This flow is a simplified model of thermal convection of water in a cavity heated from below with heat loss at its free surface. Analysis of the flow statistics suggests similarities in spatial structures to classical turbulent Rayleigh-Bénard Convection but with turbulent fluctuations near the free-slip boundary. One important observation is the asymmetry in the thermal boundary layer heights at the lower and upper boundaries. Similarly, the budget of the turbulent kinetic energy shows different behaviour at the free-slip and at the lower wall. Interestingly, the work of the mean pressure is dominant due to the hydrostatic component of the mean-pressure gradient but also depends on the density fluctuations which are small but critically, non-zero. As expected the boundary-layer heights decrease with the Rayleigh number, due to increased turbulence intensity. However, independent of the Rayleigh number, the height of the thermal boundary layer at the upper boundary is always smaller than that on the lower wall.

1. Introduction

In this paper we report on direct numerical and large-eddy simulations of turbulent thermal convection without invoking the Oberbeck-Boussinesq

approximation. The working medium is liquid water and we employ a pseudo-Rayleigh-Bénard Convection set-up with a free-slip upper boundary condition. This serves as a simplified model of the thermal convection occurring in a cavity heated from below with evaporation at its free surface. Buoyancy-driven flows due to temperature and/or concentration gradients are studied extensively in earth sciences (oceanography, atmospheric sciences and geology) but they are also encountered in diverse technological applications. One example is the turbulent thermal convection in spent-fuel pools at nuclear facilities. The principle role of a spent-fuel pool is to safely store hot fuel assemblies for the short to medium term. Under normal operation, decay heat is evacuated via a system of pumps and external heat exchangers. In the event of a loss-of-cooling accident and prolonged station black-out in a spent-fuel pool, such as that which occurred at Fukushima 2011, these systems cease to be available. Heat is then predominantly evacuated via evaporation at the free surface (more than 80% of the surface heat flux is due to latent heat transfer [1–3]). The important aspects of the occurring thermal convection can be numerically simulated by considering the upper volume of the pool only. The domain is then a cavity heated from below with a free surface as an evaporating horizontal upper boundary.

If an initially quiescent velocity field is assumed, evaporation at the free surface would induce motion in the cavity below through evaporative cooling [1–6]. Further, when heat is added from below, a natural convection flow is induced, similar to turbulent Rayleigh-Bénard Convection (RBC).

Turbulent RBC is most commonly studied numerically by invoking the Oberbeck-Boussinesq approximation for a fluid uniformly heated from below and cooled from above with solid upper and lower boundaries [7–11]. This type of flow will be henceforth referred to as *classical turbulent RBC*. The flow and thermal dynamics are then determined by the geometry of the cavity, the temperature difference across it and the resulting variation in fluid properties. The two dimensionless parameters that then govern the flow are the Prandtl number, $Pr = \hat{\nu}/\hat{\kappa}$, and the Rayleigh number, $Ra = |\hat{\mathbf{g}}|\hat{\beta}\Delta\hat{T}\hat{H}^3/(\hat{\nu}\hat{\kappa})$. In these expressions, $|\hat{\mathbf{g}}|$ is the magnitude of gravitational acceleration, $\hat{\beta}$ the thermal expansion coefficient, \hat{H} the height of the domain, $\hat{\nu}$ the kinematic viscosity, $\Delta\hat{T}$ the temperature difference between the lower and upper ($\hat{T}_L - \hat{T}_U$) boundaries and $\hat{\kappa}$ is the thermal diffusivity. The system response to a given Ra and Pr is measured in terms of the dimensionless numbers for heat flux and turbulence; respectively the Nusselt Nu and Reynolds Re numbers, where the velocity for the latter is representative of the large-scale circulation.

Although it is noted that Bénard's initial experiments were carried out with an upper boundary open to atmosphere [12], the vast majority of numerical and experimental work has concentrated on the container bounded by upper and lower walls; see [13–15] and references therein.

As a first attempt to understand the effects of the free surface on turbulent RBC, we carry out a Direct Numerical Simulation (DNS) at $Ra = 10^7$ and a series of Large-Eddy Simulations (LES) up to $Ra = 10^9$ where the free surface is approximated as a free-slip upper boundary. We further allow for variations of the density and other fluid properties by using a low-Mach number solver. To the authors' knowledge, this type of flow has not been investigated before.

A literature review suggests the most similar study to the flow examined herein is [16], in which the authors studied numerically the turbulent convection occurring in warm shallow ocean during adverse weather events. A heat flux was implemented at the free-slip upper surface to represent evaporation and the lower boundary was a rigid wall. The main two differences between [16] and our study are the increased $\Delta\hat{T}$, the unstably stratified initial condition and the energy conservation introduced here by the fixed temperatures at the upper and lower boundaries (which also implies fixed $\Delta\hat{T}$).

The Oberbeck-Boussinesq approximation assumes that density variations have no effect on the fluid properties or on the flow field other than the buoyancy force. Accordingly, the density is assumed to be constant in all terms of the governing equations except in the gravitation term. This simplifies greatly the system of equations to be solved but remains valid for only small variations in temperature [17,18]. The experimental pursuit of higher Rayleigh numbers

has inevitably resulted in increasing $\Delta\hat{T}$, larger density variations and, with it, deviations away from the validity of the Oberbeck-Boussinesq approximation. This deviation is known as the non-Oberbeck-Boussinesq effect of the working fluid. Ahlers *et al.* [19] showed that, although variable viscosity and thermal diffusivity effect boundary layer heights and temperature profiles in turbulent RBC, both Nu and Re , based on large-scale circulation velocity, are insensitive to such non-Oberbeck-Boussinesq effects, even with a $\Delta\hat{T} = 40$ K.

In this paper we take into account variable fluid properties to ensure that other qualitative flow features are not lost. Moreover, the effect of variable fluid properties on the different components of Nu , which includes the vertical turbulent heat flux, merits further attention. Finally, allowing for density variation allows for a more comprehensive analysis of the budget of the turbulent kinetic energy.

Our paper is structured as follows. The governing equations and numerical set-up are described further in §2, where we provide justifications for the DNS and LES grid resolutions. The numerical results are presented in §3, where the global structure of the moderate Rayleigh number flow is first analyzed, comparisons with the LES are made and a turbulent kinetic energy budget is provided. We then present the results of the LES at higher Rayleigh numbers and assess the impact of the non-Oberbeck-Boussinesq and free-slip conditions on the first and second-order flow statistics. Finally, conclusions are drawn in §4.

2. Governing equations and numerical set-up

The working fluid is liquid water, treated as Newtonian, at a mean temperature of 333.15 K corresponding to $Pr = 3$. Further, a $\Delta\hat{T}$ of 20 K is applied between the lower wall and upper free-slip boundary. This corresponds to a free surface temperature relevant to a loss-of-cooling accident in a spent-fuel pool during the heat-up stage of the accident [20]. The significant changes in fluid properties over the thermodynamic range of interest must be taken into account as, with water as the working fluid, the $\Delta\hat{T}$ used could render the use of the Oberbeck-Boussinesq approximation questionable [17,18]. For this reason, the system of governing equations is the low-Mach number approximation of the compressible Navier-Stokes-Fourier equations [21,22], which reads in dimensional form,

$$\frac{\partial \hat{p}}{\partial \hat{t}} + \hat{\nabla} \cdot (\hat{\rho} \hat{\mathbf{u}}) = 0, \quad (2.1)$$

$$\frac{\partial (\hat{\rho} \hat{\mathbf{u}})}{\partial \hat{t}} + \hat{\nabla} \cdot (\hat{\rho} \hat{\mathbf{u}} \hat{\mathbf{u}}) = \hat{\nabla} \cdot \hat{\boldsymbol{\tau}} - \hat{\nabla} \hat{p} + \hat{\rho} \hat{\mathbf{g}}, \quad (2.2)$$

$$\frac{\partial (\hat{\rho} \hat{c}_p \hat{T})}{\partial \hat{t}} + \hat{\nabla} \cdot (\hat{\rho} \hat{\mathbf{u}} \hat{c}_p \hat{T}) = \hat{\nabla} \cdot (\hat{\lambda} \hat{\nabla} \hat{T}) + \frac{d\hat{p}_0(t)}{d\hat{t}}, \quad (2.3)$$

where $\hat{\mathbf{u}} = (u, v, w)$. In (2.2), \hat{p} stands for the sum of the 2nd-order term of the low-Mach-number expansion of the pressure and the bulk viscous pressure [23,24]. The deviatoric part of the viscous stress tensor, $\hat{\boldsymbol{\tau}}$, is given below where \mathbf{I} is the identity matrix and $\hat{\mu}$ the dynamic viscosity,

$$\hat{\boldsymbol{\tau}} = \hat{\mu} \left(\hat{\nabla} \hat{\mathbf{u}} + (\hat{\nabla} \hat{\mathbf{u}})^T - \frac{2}{3} (\hat{\nabla} \cdot \hat{\mathbf{u}}) \mathbf{I} \right). \quad (2.4)$$

In (2.3), \hat{c}_p is the specific heat, $\hat{\lambda}$ the thermal conductivity and $\hat{p}_0(t)$ the 1st-order component of the asymptotic expansion of pressure at the zero-Mach limit, interpreted as the thermodynamic pressure. According to the low-Mach number expansion, it is spatially uniform and a function of time only. For open domains, \hat{p}_0 is equal to the ambient pressure. For closed domains it varies with time and can be computed from the equation of state of the working medium [22]. In our study the domain is closed; however preliminary computations showed that the variations of \hat{p}_0 are negligibly small. For this reason, in our simulations \hat{p}_0 is set equal to the ambient pressure of one atmosphere.

In order to close the system of governing equations, we introduce a $\hat{\rho} - \hat{T}$ relation, i.e. an isobaric “equation of state”, for water density. This relation is a fourth-order polynomial fit, (2.5), of the tabulated data in [25] for water density at one atmosphere and over the temperature range of interest, 323.15K to 343.15K. The coefficients of the polynomial fit are provided in table 1. According to (2.5), the liquid density varies by 1% over the range of interest. All other fluid properties are also calculated from a quartic polynomial of the form (2.5) with corresponding coefficients given in table 1.

$$\phi = c_4 \hat{T}^4 + c_3 \hat{T}^3 + c_2 \hat{T}^2 + c_1 \hat{T} + c_0. \quad (2.5)$$

The dynamic viscosity, $\hat{\mu}$, and the thermal conductivity, $\hat{\lambda}$, vary respectively by 35% and 3 % over the temperature range of interest. In other words, even though the density variations are small, the induced variations in the transport properties of water are significant. On the other hand, the specific heat, \hat{c}_p , varies by only 0.2% over the domain and is thus taken as constant in the simulations. It is noted however that, as a result of the aforementioned variations of the fluid properties, Pr varies by 40% across the domain.

Table 1. Polynomial coefficients for variable fluid properties.

	c_4	c_3	c_2	c_1	c_0
$\frac{\hat{\rho}}{\hat{\rho}_0}$	-2.87×10^{-12}	3.92×10^{-09}	-2.038×10^{-06}	4.7×10^{-04}	-0.031
$\hat{\mu}$	1.10×10^{-11}	-1.57×10^{-08}	8.43×10^{-06}	-2.03×10^{-03}	0.185
$\hat{\lambda}$	3.6×10^{-11}	-3.4×10^{-08}	2.2×10^{-06}	5.4×10^{-03}	-0.59

The reference values of the fluid properties at $\hat{T}_m = 333.15$ K are $\hat{\rho}_{\text{ref}} = 983.2 \text{ kg/m}^3$, $\hat{c}_{p,\text{ref}} = 4183 \text{ J/kg K}$, $\hat{\lambda}_{\text{ref}} = 0.65 \text{ W/m K}$, and $\hat{\alpha}_{\text{ref}} = 1.6 \times 10^{-7} \text{ m}^2/\text{s}$. These are later used for non-dimensionalization purposes along with the other Ra dependent variables provided in table 2. Wherein, $\hat{U}_f = (|\hat{\mathbf{g}}| \hat{H} \hat{\beta} \Delta \hat{T})^{\frac{1}{2}}$ is the free-fall velocity, later used to calculate the free-fall time from $\hat{t}_f = \hat{H} / \hat{U}_f$.

Table 2. Non-dimensionalisation parameters.

Ra	$\hat{H}(m)$	$\hat{U}_{\text{ref}}(\frac{m}{s})$
10^7	0.019	$\hat{U}_f = 0.045$
10^8	0.041	$\hat{U}_f = 0.066$
10^9	0.090	$\hat{U}_f = 0.096$

All dimensional variables have been denoted with a hat symbol $\hat{\cdot}$ and dimensionless variables are denoted without it. Henceforth, we will use uniquely non-dimensional variables and the normalized temperature, $\theta = (\hat{T} - \hat{T}_m) / \Delta \hat{T}$. The domain is a (1:1:6) cuboid with the unity aspect ratio corresponding to the first horizontal (x) and vertical (y) directions. The second longitudinal (z) direction is periodic with a length of $L = 6$. The lower wall is located at $y = 0$, the upper boundary at $y = 1$ and, likewise, the side walls at $x = 0$ and $x = 1$ respectively.

The side walls are assumed to be adiabatic; as such, the condition $\frac{\partial \theta}{\partial x} = 0$ is prescribed at them. The lower (hot) and upper (cold) walls are isothermal and kept at $\theta = 0.5$ and $\theta = -0.5$ respectively. No-slip velocity boundary conditions are enforced at the side and lower walls, whereas the free-slip condition is prescribed at the upper-boundary, i.e. $\frac{\partial u}{\partial y} = \frac{\partial w}{\partial y} = 0$ and $v = 0$ at $y = 1$. As a result of the aforementioned boundary conditions there are three hydrodynamic boundary layers, one at each the vertical side walls and one at the lower wall. On the other hand, there are only two thermal boundary layers, one each at the lower wall and upper boundary.

With regard to initial conditions for the DNS, we employ a linear temperature profile across the vertical and a quiescent velocity field to which we apply small random perturbations. This initially unstable stratification results in the formation of convective patterns which then break down into turbulent motion until a statistically steady state is reached.

We run simulations for 100 free-fall times before assuming a statistically steady state has been reached. This is sufficient time to wash out all transient effects [11]. Subsequently, averages are taken over a further 200 free-fall times, which is a longer averaging period than that used in [26] for the DNS of classical turbulent RBC at the same Ra and in a similar set-up. The criterion for determining whether sufficient statistical data has been taken is elaborated on in section 3. Regarding the initial conditions for the LES at $Ra = 10^7$ and $Ra = 10^8$, the temperature and velocity fields are initialized from the DNS solution. Likewise, the flow fields for the LES at $Ra = 10^9$ are initialized from the LES solution of $Ra = 10^8$.

For the numerical solution of (2.1) - (2.3) we employ a second-order accurate time-integration scheme for convective and diffusive terms taking into account the current and the two previous time steps. Regarding the spatial discretization, the governing equations are discretized using second-order central difference schemes on a collocated grid system. A flux interpolation technique is used in the spirit of Rhie and Chow [27], to avoid pressure odd-even decoupling [28].

For the pressure-velocity coupling a PISO-type projection method is used, similar to [29] and [30] for incompressible flows. The divergence of the momentum equation is taken and the continuity equation is used as a constraint to formulate the variable-coefficient Poisson equation to be solved for \hat{p} . In this low-Mach-number PISO algorithm, a $\frac{\partial \hat{p}}{\partial t}$ emerges on the left-hand side of the Poisson equation which would be zero for the incompressible case. A similar OpenFOAM[®] algorithm is developed in [31].

(a) DNS resolution requirements

An accurate DNS necessitates the resolution of the smallest length scales of the flow in both the bulk and the boundary layers. An a priori method for checking the grid resolution in the bulk of the domain is provided in [11], based originally on [32]. To this end, we recall that the dimensionless Kolmogorov scale η is defined as $\eta = (\nu^3/\epsilon_u)^{\frac{1}{4}}$ with ϵ_u being the dimensionless kinetic-energy dissipation. Also, the Batchelor scale is $\eta_\theta = (\kappa^3/\epsilon_\theta)^{\frac{1}{4}}$ with ϵ_θ being the dimensionless thermal dissipation. Now, let h be the maximum length of a given computational cell in the inhomogeneous direction, that is $h = \max(\Delta x, \Delta y)$. When $Pr > 1$, which is the case for the flows under study, the maximum wavenumber seen by the grid, $k_{\max} = \pi/h$, must be greater than the reciprocal of the Batchelor scale [11,32]. The combination of the above relations leads to the following restriction,

$$h \leq \pi \eta_\theta = \pi \left(\frac{\kappa^3}{\epsilon_\theta} \right)^{\frac{1}{4}}. \quad (2.6)$$

Using the argument of Deardroff and Willis [33] that the turbulent kinetic energy (TKE) dissipation profile in classical turbulent RBC is flat in the bulk of the flow, Grötzbach [32] then assumes this TKE dissipation to be constant and equal to the buoyant production. If an equivalent argument holds for the thermal dissipation, then the above restriction for the Batchelor scale is transformed into (2.7), referred to herein as the “thermal resolution requirement”. This method is only valid for homogeneous isotropic turbulence but is considered a reasonable a priori prediction for adequate resolution in the bulk of the domain.

The resolution requirement based on the smallest hydrodynamic (Kolmogorov) scale is also given in (2.8), and is referred to herein as the “hydrodynamic resolution requirement”. Although (2.8) is less restrictive for the case studied, we use it later to elaborate on the choice of grid resolution for our LES,

$$h \leq \pi \eta_\theta = \pi \left(\frac{1}{Ra Pr Nu} \right)^{\frac{1}{4}}, \quad (2.7)$$

and

$$h \leq \pi \eta = \pi \left(\frac{Pr^2}{Ra Nu} \right)^{\frac{1}{4}}. \quad (2.8)$$

Clearly, (2.7) and (2.8) require an estimation of Nu in advance. To the authors knowledge, there are no correlations in the literature for the system studied here, hence the refinement procedure can be seen as an iterative process. We first use a correlation for classical turbulent RBC such as [34] to provide an estimation for Nu , which is then updated a posteriori in (2.7) and the bulk resolution recalculated. The final DNS grid spacing in the vertical (and horizontal) direction is shown in figure 1 along with estimates of the Batchelor (2.7) and Kolmogorov (2.8) requirements at $Ra = 10^7$. The cells are clustered near the walls to capture the sharp gradients in temperature and velocity. At $Ra = 10^7$ the soft turbulence regime exists [35], where it is known that hot plumes leaving the lower heated boundary traverse the entire cavity and impact the upper cooled boundary and vice versa. Resolving the associated scales is important to resolving the overall structure of the flow. Hence, the grid is non-uniform throughout the cavity, as recommended in [36].

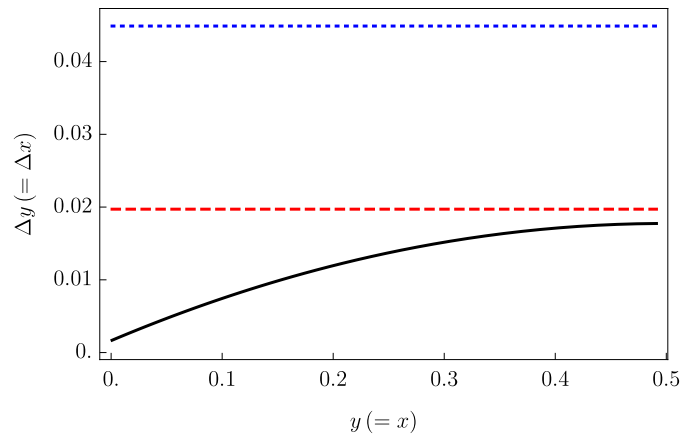


Figure 1. Vertical and horizontal grid resolution for the DNS at $Ra = 10^7$: actual resolution (—), global estimation of thermal resolution requirement (---) and global estimation of hydrodynamic resolution requirement (⋯⋯). Only half the domain is shown due to symmetry.

In classical turbulent RBC, the turbulent kinetic energy dissipation peaks close to the hydrodynamic boundary layers. It is therefore important to ensure that the grid is most refined at the boundaries. We choose to refine the vertical and horizontal directions using a hyperbolic-tangent expansion from the minimum cell size at the boundaries to the maximum in the centre of the cavity.

The second resolution criterion is to ensure that the hydrodynamic and thermal boundary layers are well-resolved. Shiskina *et al.* [37] developed a universal criterion based on the laminar Prandtl-Blasius boundary layer theory. The a priori estimates for the dimensionless heights of δ_u and δ_θ are given by

$$\delta_u = 0.5 Nu^{-1} Pr^{\frac{1}{3}} E^{-1}, \quad (2.9)$$

$$\delta_\theta = \delta_u E Pr^{\frac{1}{3}}. \quad (2.10)$$

Then, according to [37], the minimum resolution requirements for $\delta_{\mathbf{u}}$ and δ_{θ} , denoted by $N_{\mathbf{u}}$ and N_{θ} respectively, are

$$N_{\mathbf{u}} = \sqrt{2}aNu^{\frac{1}{2}}Pr^{\frac{1}{3}}E^{\frac{1}{2}} \approx 5, \quad (2.11)$$

$$N_{\theta} = \sqrt{2}aNu^{\frac{1}{2}}E^{\frac{3}{2}} \approx 4, \quad (2.12)$$

where a and E are empirical constants with $a = 0.482$ and $E = 0.982$. For the flow under study, we then have that $N_{\mathbf{u}} = 5$ and $N_{\theta} = 4$.

As shown in table 3, the above estimations are taken as *minimum* requirements for the number of points inside the boundary layers, i.e. the boundary layers are intentionally over-resolved. The values inside parentheses in the N_{θ} and $N_{\mathbf{u}}$ columns correspond to the minimum resolution requirements. A qualitative definition of the N_y in table 3 is the minimum number of points required in the vertical direction to satisfy both the grid-resolution requirements in bulk [11] and in the boundary layers [37].

This results in $\Delta y_{\max} = \Delta x_{\max}$ in the centre of the cavity. For the DNS, the uniform longitudinal grid resolution is determined from the maximum cell height (and width) found in the centre, that is $\Delta z = \Delta y_{\max} = \Delta x_{\max}$, used to calculate N_z from $\frac{L}{\Delta z}$.

Table 3. DNS grid resolution criteria. The numbers in parentheses correspond to the minimum resolution requirements.

Ra	N_{θ}	$N_{\mathbf{u}}$	N_x	N_y	N_z
10^7	13 (4)	10 (5)	110	110	360

For the computation of the time increment in our simulations, we set the Courant number equal to 0.25. As pointed out in [26] the constraint on the time-step for numerical stability purposes is stricter than that of the Kolmogorov (and Batchelor) timescales; we can therefore assume that the smallest of the flow timescales are well captured.

(b) LES resolution requirements

The use of LES for the highest Rayleigh numbers is motivated by computational limitations. In this study we decide first to carry out the DNS at $Ra = 10^7$ and then compare statistics with a LES of the same Ra but using a coarse mesh, where cell numbers are reduced by approximately a factor of 3 in each direction. Once comparisons of flow statistics suggest satisfactory predictions by the LES at moderate Ra , we apply similar refinement criteria to the meshes at higher Ra . This task is complicated by the further requirement for the minimum number of points in the thermal, N_{θ} , and hydrodynamic, $N_{\mathbf{u}}$, boundary layers outlined above. The procedure is summarized in four steps: (i) determine the boundary-layer and bulk resolution requirements for the DNS at the chosen Ra , (ii) reduce by a factor of 3 the number of points in the vertical and horizontal, (iii) increase the hyperbolic-tangent expansion in a manner that guarantees the boundary-layer requirements are met and, finally, (iv) set $\Delta z = \Delta y_{\max} = \Delta x_{\max}$.

In all LES presented herein the number of points in the boundary layers exceeds the requirement in [37], whereas the bulk resolution requirement is relaxed by approximately a factor of 4. Consequently, the difference between the smallest and largest cells, $\Delta y_{\max}/\Delta y_{\min}$, for the LES is approximately 40. An alternative LES resolution requirement is to match the filtering cut-off width to the Taylor microscale, which for isotropic turbulence is defined as $\eta_l = (15 \nu \mathbf{u}^2 / \epsilon_{\mathbf{u}})^{\frac{1}{2}}$ [38], where \mathbf{u} is a representative velocity of the large structures. With appropriate scaling for $\epsilon_{\mathbf{u}}$, Peng *et al.* [39] uses the relation (2.13) for half the Taylor microscale where \mathbf{u}^* is found from (2.14) using the turbulent RBC scaling relations of [7],

$$\frac{\eta_l}{2} = \frac{\sqrt{15}\mathbf{u}^*}{[Ra(Nu-1)]^{\frac{1}{2}}}, \quad (2.13)$$

$$\mathbf{u}^* = \sqrt{0.0027Ra^{1.04} + 0.0312Ra^{0.92}}. \quad (2.14)$$

This procedure gives a good approximation of an a priori LES bulk resolution requirement. In-line with [39] we choose to use half the Taylor microscale, $\frac{\eta_l}{2}$, as a maximum cell size found in the bulk. The above values are summarized in table 4 and an example resolution is shown graphically for $Ra = 10^8$ in figure 2, where the maximum bulk cell size lies between that of the hydrodynamic resolution requirement ((2.8)) and half the Taylor microscale ((2.13)).

Table 4. LES grid resolution criteria. The numbers in parentheses correspond to the minimum resolution requirements.

Ra	N_θ	N_u	N_x	N_y	N_z	$\frac{\Delta y_{\max}}{\Delta y_{\min}}$	$\frac{\pi\eta_\theta}{\Delta y_{\max}}$	$\frac{N_{\text{DNS}}}{N_{\text{LES}}}$	$\frac{\eta_l}{2}$
10^7	6 (4)	7 (5)	40	40	100	40	3.5	37	0.051
10^8	7 (5)	9 (7)	80	80	200	35	3.5	36	0.034
10^9	9 (7)	11 (9)	130	130	300	45	4.5	40	0.023

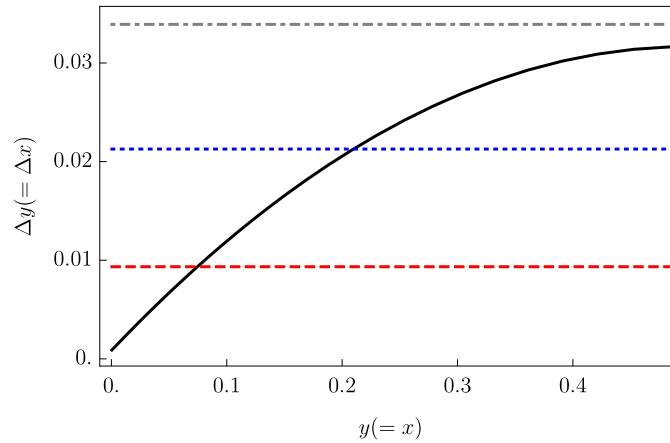


Figure 2. Vertical and horizontal grid resolution for the LES at $Ra = 10^8$: actual resolution (—), global estimation of thermal resolution requirement (---), global estimation of hydrodynamic resolution requirement (.....) and half the Taylor microscale or $\frac{\eta_l}{2}$ (-.-.). Only half the domain is shown due to symmetry.

Following this procedure means that the LES is well-resolved at the walls, and hence no wall model is required. However, in the bulk, the LES mesh described above resolves only the large-scale structures. The effects of the unfiltered small scales must therefore be captured by an appropriate subgrid-scale model. These effects can be modelled as subgrid-scale viscous stresses and a subgrid-scale heat flux, respectively, in the momentum and energy equations.

For the subgrid-scale stresses the eddy viscosity μ_t is introduced so that the effective viscosity, $\mu_{\text{eff}} = \mu + \mu_t$, replaces μ in (2.4). In this study, the Langrangian dynamic subgrid-scale model [40] is used to dynamically calculate μ_t , which allows for the inhomogeneity of the flow within a (partial) container to be captured.

Similarly, for the subgrid-scale heat flux, the eddy diffusivity λ_t is introduced and the effective thermal conductivity, $\lambda_{\text{eff}} = \lambda + \lambda_t$, then replaces λ in (2.3). In our study, λ_t is computed from

the local μ_t and ρ and by assuming a constant value of the turbulent Prandtl number, $Pr_t = 0.9$ [23,41].

3. Numerical results

The numerical results are presented in two parts. First, the moderate Rayleigh number case, at $Ra = 10^7$, is analyzed by looking at the mean flow properties, instantaneous flow structures, comparisons of second and third-order flow statistics between the LES and DNS and a turbulent kinetic energy budget of the DNS. We then look at the time-averaged flow properties and flow statistics of the LES over increasing Ra and quantify the effects of the free-slip boundary and variable fluid properties. Unless stated otherwise the notation adopted is as follows; the mean of a generic variable ϕ is denoted by $\langle \phi \rangle$ and refers to averaging both in time and over the homogeneous (periodic) z direction. The fluctuating component is denoted by ϕ' and the root mean square (rms) value by $\phi_{rms} = \langle \phi' \phi' \rangle^{1/2}$.

(a) Analysis of moderate-Rayleigh-number flow

We start with the presentation and analysis of the flow at the moderate Rayleigh number of 10^7 .

(i) Mean flow properties

We first look at the the spatial resolution of the DNS. We confirmed that the grid resolution criterion (2.6), $\frac{h}{\pi \eta \theta} \leq 1$, is appropriately met so that the hydrodynamic and thermal resolution requirements of the flow are satisfied. Other methods for assessing the grid quality are also available. For example, Davidson [42] has proposed to verify the grid resolutions on the basis of the computed dissipation spectra. Herein, however, we opted for criterion (2.6), which is also the typical choice for simulations of thermal convection [11].

A first understanding of the statistical steadiness of the solution can be obtained from analysis of the heat transfer in the domain. The non-dimensional heat transfer across the $x - z$ plane is measured by the local Nusselt number, Nu_y , calculated from (3.1). This relation is found from time and area-averaging of the nondimensionalised form of the energy equation (2.3). The volume-averaged (global) Nusselt, Nu_G , is found from (3.2).

$$Nu_y = \underbrace{\sqrt{RaPr} \langle \rho v \theta \rangle_{xzt}}_{Nu_{conv}} - \underbrace{\langle \lambda \frac{\partial \theta}{\partial y} \rangle_{xzt}}_{Nu_{diff}}, \quad (3.1)$$

$$Nu_G = \sqrt{RaPr} \langle \rho v \theta \rangle_{xyzt} - \langle \lambda \frac{\partial \theta}{\partial y} \rangle_{xyzt}. \quad (3.2)$$

In the above equations, the symbol $\langle \rangle_{xzt}$ denotes averaging over time and over a given horizontal $x - z$ plane, whereas the symbol $\langle \rangle_{xyzt}$ denotes averaging over time and volume. For the flow in question, a statistically steady solution will give Nu_y as constant for $0 \leq y \leq 1$ and further equal to Nu_G . For the DNS here $Nu_y = Nu_G = 21.4$. Further, its value changes by less than 0.1% if only the first half of the averaging time is used suggesting that a statistically steady state has indeed been reached.

For the LES, an effective thermal conductivity, λ_{eff} , replaces λ in (3.1) and (3.2) due to the additional turbulent contribution. Also, regarding the LES, $Nu_y = 19.9$ and $Nu_G = 20.0$, which corresponds to an underprediction of approximately 7% when compared to the DNS. We note that in previous studies of RBC using LES such as [43], Nu is *over*-predicted when compared to experimental and DNS data. It is known that underresolved boundary layers result in an overprediction of Nu [7,11], we therefore postulate that the errors in the prediction of the LES are not due to low resolution but most likely related to the constant turbulent Prandtl number Pr_t used in this study. This is an aspect to be improved in future studies.

The vertical distribution of Nu_y for both the DNS and the LES are now assessed. The differing contributions of the convective and diffusive components of Nu_y are shown in figures 3a and 3b respectively. Only half of the domain is shown for the convective component which tends to a non-zero but negligible value inside the boundary layers. For the diffusive component only the boundary layer is shown, as it is negligible in the bulk.

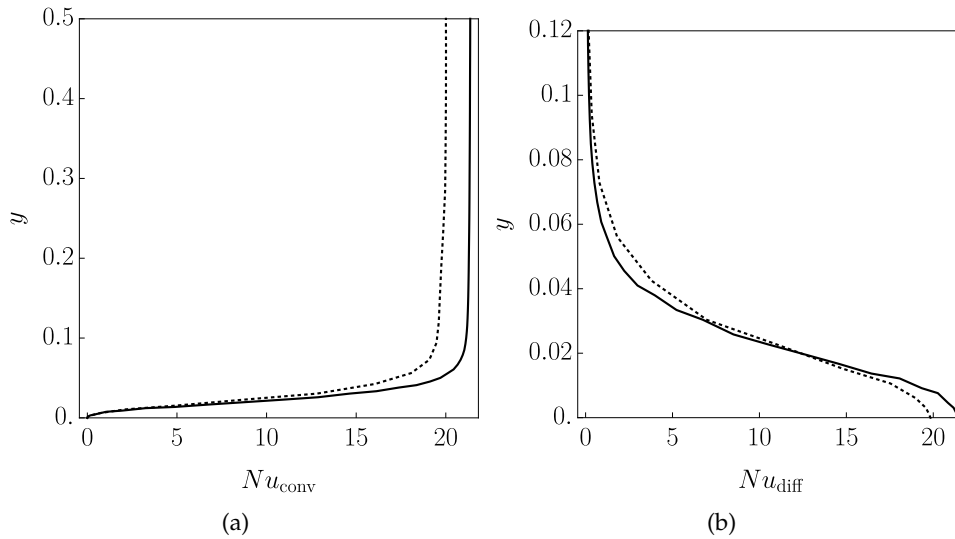


Figure 3. Plots of the time and area-averaged components of Nu_y at $Ra = 10^7$. (a) Nu_{conv} across the lower half of the domain and (b) Nu_{diff} zoom on lower boundary. The legend is as follows: DNS (—) and LES (.....).

We note that a constant Nu is a necessary but not sufficient condition to ensure a statistically steady solution. A better indication of steadiness is found by looking at the time derivative term of the turbulent kinetic energy equation, completed later on in this section.

The DNS at $Ra = 10^7$ is now qualitatively assessed in order to obtain a global understanding of the flow. Time-averaged streamlines are shown in figure 4 coloured by the non-dimensional vertical velocity v . The cuboid geometry means that a typical diagonal large-scale circulation is observed, such as in [44]. However, due to the extension of the domain in the homogeneous z direction, multiple large-scale circulation patterns are formed. Three individual large-scale circulations can be identified as contained and the fourth appears across the periodic boundary.

A diagonal plane of the first contained large-scale circulation is shown in figure 4 and a zoom is provided in figure 5. The typical large-scale-circulation for RBC in a cubic container is observed in the superimposed velocity vectors, i.e. the large-scale circulation fills the entirety on the vertical domain with recirculation zones in the corners corresponding to peaks in the θ_{rms} [44]. The same pattern is observed over all three contained mean winds except that the direction of the large-scale circulation is reversed.

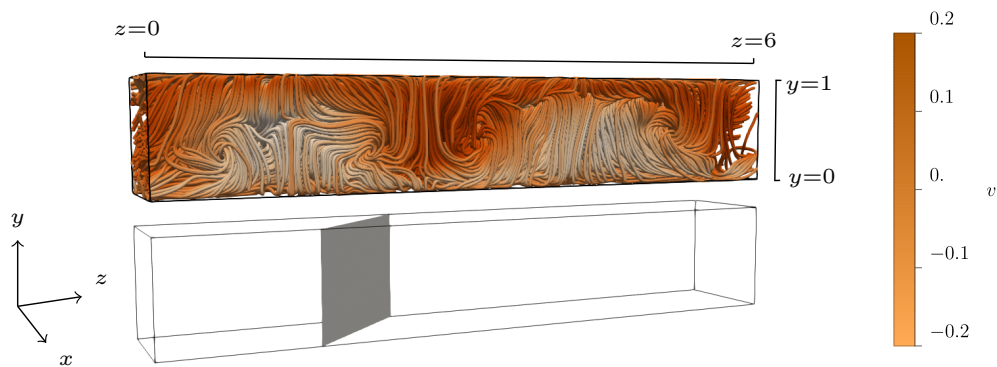


Figure 4. Time-averaged streamlines of DNS at $Ra = 10^7$ coloured by non-dimensional vertical velocity, v .

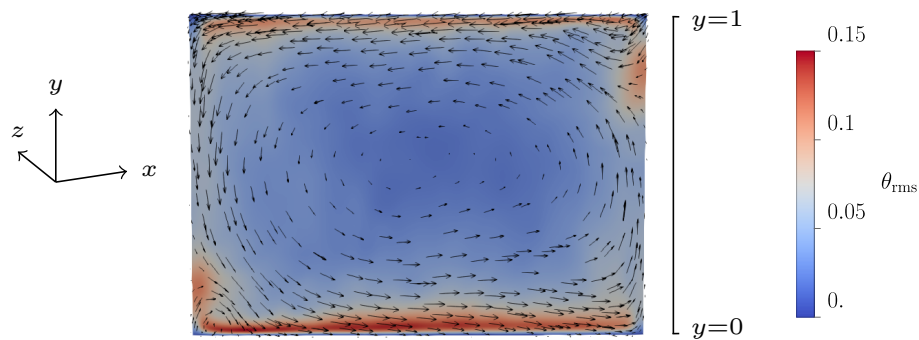


Figure 5. Colour plot of θ_{rms} with superimposed velocity vectors of the DNS at $Ra = 10^7$. The location of the diagonal plane is provided in figure 4

(ii) Instantaneous structures

The instantaneous normalized temperature at the central $y - z$ plane is provided in figure 6 where thermal plumes are visible. A zoom on two such plumes is given in figure 7, one warm rising (red) and one cold falling (blue) which are seen to be extending across the entire vertical domain, i.e. from one thermal boundary layer to the other. This flow behaviour is symptomatic of the soft turbulence regime that still exists for the case of $Ra = 10^7$ [7,35].

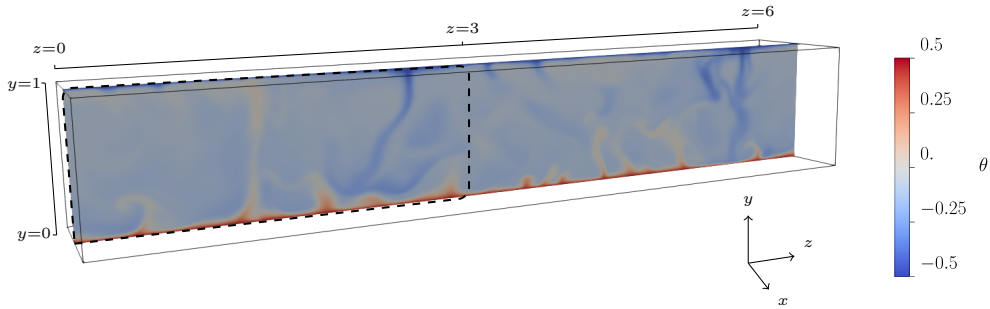


Figure 6. Colour plot of the instantaneous normalized temperature θ of the DNS at $Ra = 10^7$. The y - z plane is located at $x = 0.5$.

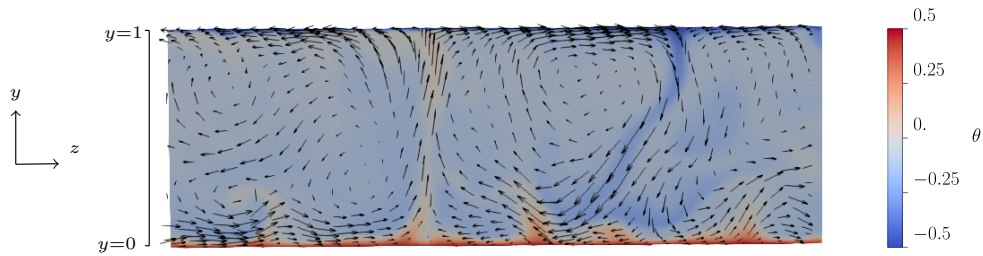


Figure 7. Colour plot of the instantaneous normalized temperature θ with superimposed velocity vectors of the DNS at $Ra = 10^7$. The figure shows a zoom on the dashed section from figure 6.

(iii) Flow statistics

In this section we compare second and third-order statistics of the velocity and temperature fields at mid-width for the DNS and LES at $Ra = 10^7$. We will often compare our numerical results against those of Kerr [7] for classical turbulent RBC with periodic x and z directions. We will also make comparisons against the numerical predictions of Zikanov *et al.* [16] for Oberbeck-Boussinesq thermal convection with periodic x and z directions but with free slip at the upper boundary.

The rms plots of the vertical velocity at mid-width, $x = 0.5$, are presented in figure 8a. The observed parabolic profile shows zero v_{rms} values at the boundaries which rise steeply towards a maximum in the bulk. Overall, the profiles are similar as those for the flows examined in [7,16]. However, contrary to the profile in [7], the profile is slightly flatter in the bulk and not fully symmetric with respect to the mid-plane $x = 0.5$. This may be attributed to the variation of the fluid transport properties with the temperature, i.e. the non-Oberbeck-Boussinesq conditions. On the other hand, we note that the free-slip condition has no significant effect on the profile of v_{rms} close to the upper boundary. This is due to the zero-Neumann condition for the vertical velocity component that is prescribed at both rigid walls and free-slip boundaries.

With regard to comparisons between LES and DNS, from figure 8a we readily deduce that the LES results match closely the DNS data. However the LES slightly overpredicts the v_{rms} in the bulk of the domain.

The rms plots of the in-plane velocity,

$$\bar{u}_{\text{rms}} = \langle u'^2 + w'^2 \rangle^{\frac{1}{2}}, \quad (3.3)$$

at mid-width, $x = 0.5$, are presented in figure 8b. According to our simulations, the vertical profile shown first peaks near the lower solid boundary, followed by a significant dip in the core region before a maximum is reached at the free-slip upper boundary. This profile is similar to that in [16] but markedly different to the symmetric profile in [7]. We therefore conclude that the asymmetry in the rms of the in-plane velocity is due to the free-slip condition imposed at the upper boundary.

We see that the LES prediction agrees quite very well with the DNS results. Nonetheless, it marginally overpredicts the local peak \bar{u}_{rms} near the lower boundary. According to [7], the height of a hydrodynamic boundary layer, δ_u , is defined as the location of the local peak of the in-plane velocity variance. The DNS and LES predictions of the height of the hydrodynamic boundary layer are given in table 5 where the LES predictions are shown to be in very good agreement with our DNS data.

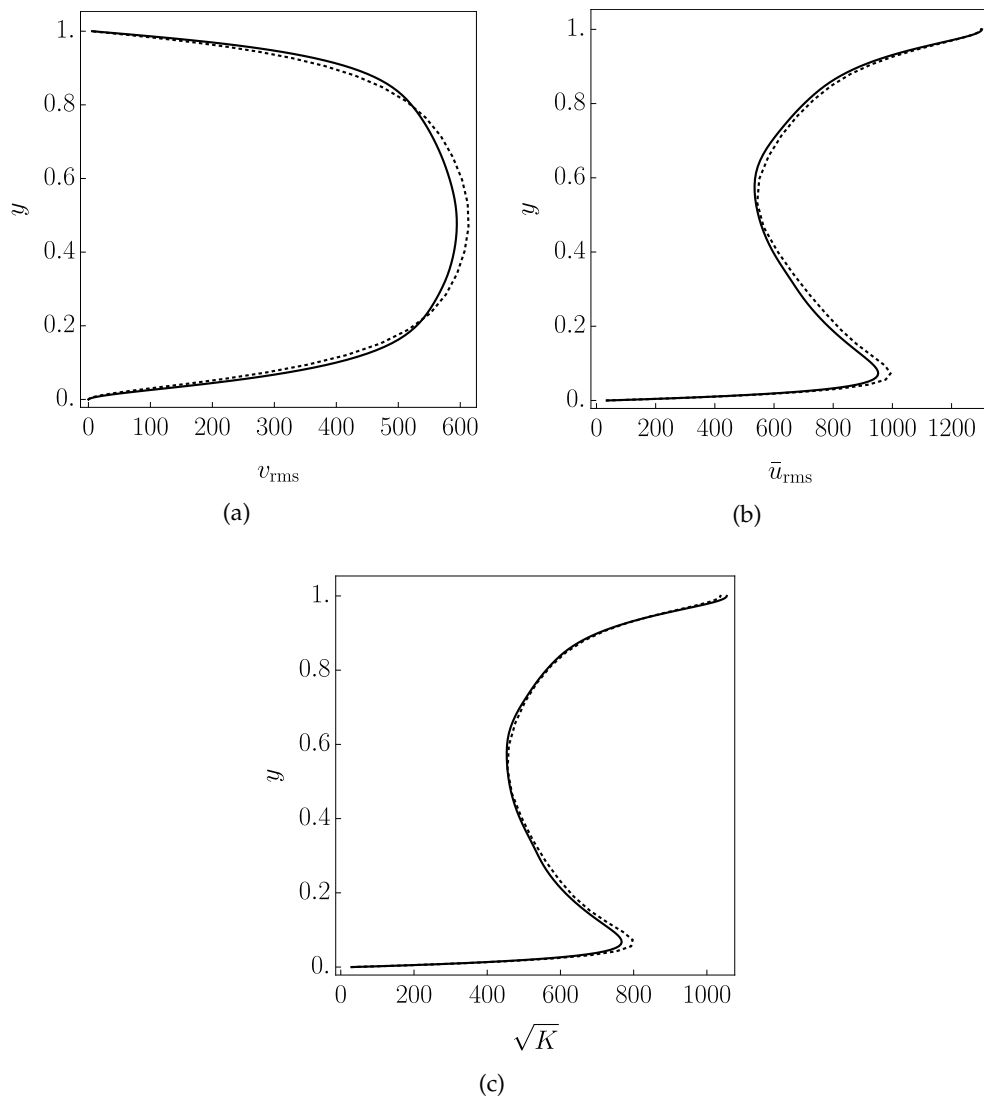


Figure 8. Velocity rms and turbulent kinetic energy plots of $Ra = 10^7$ at mid-width, $x = 0.5$. (a) vertical velocity rms, v_{rms} , (b) in-plane velocity rms, \bar{u}_{rms} and (c) square root of the turbulent kinetic energy, \sqrt{K} . The velocity has been non-dimensionalised by $\hat{\kappa}/\hat{H}$. The legend is as follows: DNS (—) and LES (.....).

The plots of the square root of the turbulent kinetic energy,

$$\sqrt{K} = \sqrt{\frac{1}{2}u_{\text{rms}}^2 + \frac{1}{2}v_{\text{rms}}^2}, \quad (3.4)$$

at mid-width, $x = 0.5$, are presented in figure 8c. According to our DNS, this profile is very similar to the that of \bar{u}_{rms} . In other words, \sqrt{K} peaks at a small distance from the lower wall and dips in bulk before it reaches its maximum at the top boundary. This is a direct consequence of the fact that, at any given y , the velocity fluctuations of the in-plane velocity are considerably higher than the ones of the vertical velocity component. On the other hand, in [7] it is reported that \sqrt{K} remains nearly constant in the bulk.

The plots of the mean normalized temperature, $\langle \theta \rangle$, along the vertical axis are presented in figure 9 where it is clear that the value at the core, θ_c , is smaller than the average, $\theta_m = \frac{1}{2}(\theta_U + \theta_L) = 0$. In other words, the mean temperature profile is “shifted towards” the temperature of the cold upper boundary. Furthermore, the height of the upper thermal boundary layer is smaller than the height of the lower one.

These characteristics are due to the competing influences of the free-slip at the upper boundary and of the variation of the fluid properties with the temperature. In fact, the authors of [19] studied RBC under non-Oberbeck-Boussinesq conditions and attributed an asymmetry to the variable viscosity and thermal diffusivity of water over the temperature range which had the overall effect of increasing the height of the upper thermal boundary layer and of decreasing the height of the lower one. However, figure 9a suggests that the overall effect is to shift θ_c in the opposite direction; in other words, in the flow under study, the effect of the free-slip on top is more important. The LES prediction agrees very well with the DNS results in the bulk with small deviations in the thermal boundary layers.

The rms plots of the normalized temperature, θ_{rms} , at $x = 0.5$ are shown in figure 10. The observed profile is that of two peaks in the thermal boundary layers with a minimum value found in the bulk. The most striking feature is the inhomogeneity in the peak values of the two thermal boundary layers and their respective distances from the boundaries. According to [7] and [45] the height of a thermal boundary layer is defined as the location of the local peak of the temperature variance. We denote by δ_{θ_L} and δ_{θ_U} the heights of the lower (hot) and upper (cold) boundaries respectively. Then, we can readily infer from figure 10, that δ_{θ_L} is larger than δ_{θ_U} , in accordance with the observations made regarding the vertical mean temperature profile at mid-width. The values of δ_{θ_L} and δ_{θ_U} are given in table 5. We confirm that, at the lower boundary, the hydrodynamic layer is substantially thicker than the thermal one, as expected for $Pr > 1$.

Table 5. Boundary layer heights at $Ra = 10^7$.

	Ra	$\delta_{\mathbf{u}_L}$	δ_{θ_L}	δ_{θ_U}	$\frac{1}{2N_u}$
DNS	10^7	0.073	0.027	0.018	0.023
LES	10^7	0.073	0.031	0.017	0.025

With regard to the LES predictions of θ_{rms} we see that they agree well with the DNS results. Most notably, the LES underpredicts θ_{rms} in the bulk and at the peak locations. Nevertheless, the trend is very well reproduced. Furthermore, the values of δ_{θ_L} and δ_{θ_U} are accurately computed, as expected from a wall-resolved LES.

Further, the last column of table 5 represents an estimation of the thermal boundary layer heights in classical turbulent RBC, $\delta_{\theta_L} = \delta_{\theta_U} = \frac{1}{2N_u}$, so that $\frac{1}{2}(\delta_{\theta_L} + \delta_{\theta_U}) = \frac{1}{2N_u}$; see e.g. [8]. In other words, this estimate assumes symmetric thermal boundary layers at the upper and lower boundaries for classical turbulent RBC. According to our simulations, the introduction of the free slip at the upper boundary suppresses the symmetry in the heights of the thermal boundary

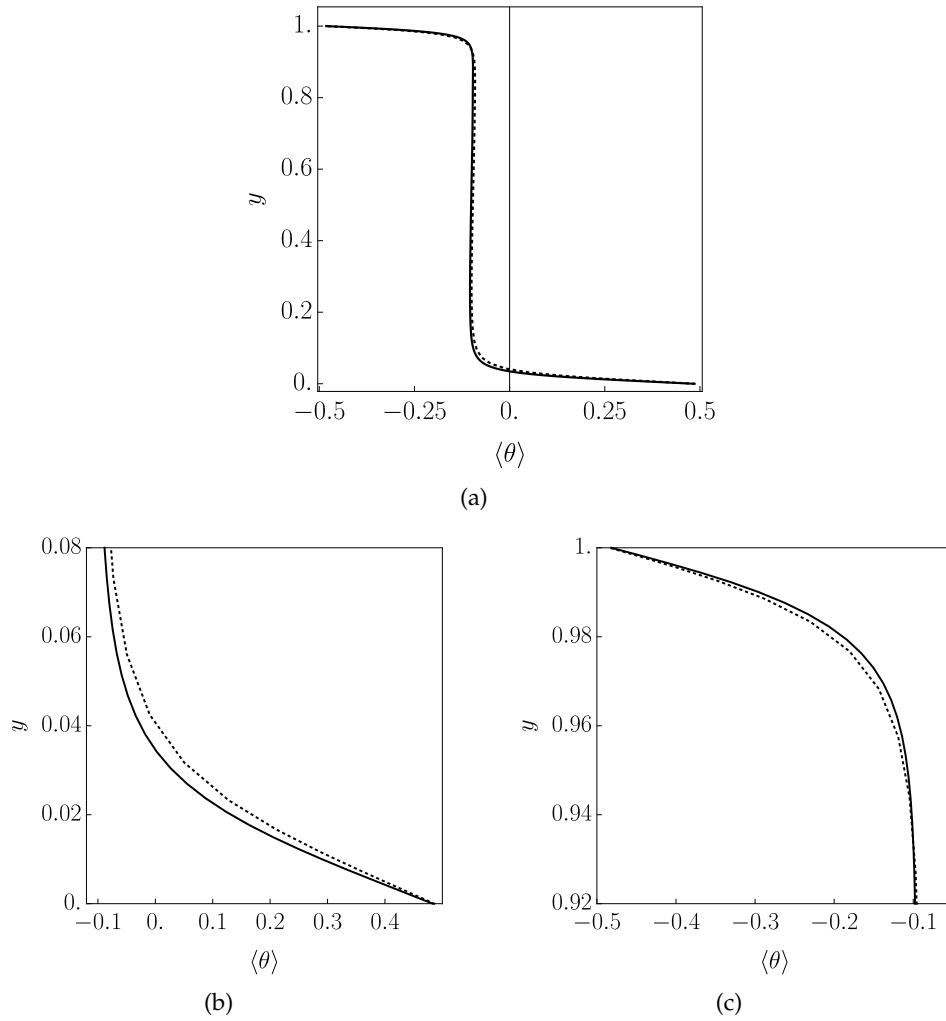


Figure 9. Mean normalized temperature, $\langle \theta \rangle$, plots of $Ra = 10^7$ at mid-width, $x = 0.5$. (a) across the vertical, (b) zoom on the lower wall and (c) zoom on the upper boundary. The legend is as follows: DNS (—) and LES (⋯⋯).

layers. However, despite this asymmetry, the relation $\frac{1}{2}(\delta_{\theta_L} + \delta_{\theta_U}) = \frac{1}{2N_u}$ remains valid for the flow under study too.

The plots of the turbulent heat flux $\langle \theta'v' \rangle$ along the y direction and at $x = 0.5$ are provided in figure 11. We observe that the profiles vary in the bulk of the domain. It is further noted that a dip in the turbulent heat flux in the bulk has also been predicted by the LES of classical turbulent RBC presented in [46]. The authors of [46] attributed this artificial dip to the low resolution of LES. However, in our case, the variation of $\langle \theta'v' \rangle$ along the vertical direction is observed in our DNS and, consequently, it cannot be a resolution artifact.

In order to explain the observed dip, we first remark that the profiles of $\langle \theta'v' \rangle_{xzt}$ for classical turbulent RBC [7] are constant in the bulk, where the subscript “ xzt ” denotes time and area-averaged quantities. Indeed, since convective transfer is dominant in the bulk thermal energy balance at steady state implies that the profile of $\langle \theta v \rangle_{xzt}$ is constant in the bulk under Oberbeck-Boussinesq conditions. Moreover, we have that $\langle \theta'v' \rangle_{xzt} = \langle \theta v \rangle_{xzt}$ by virtue of the zero divergence of the velocity field. In turn, this implies that $\langle \theta'v' \rangle_{xzt}$ is constant in the bulk. This has been observed by various authors who studied classical turbulent RBC numerically; see, for example, [39,43] and references therein.

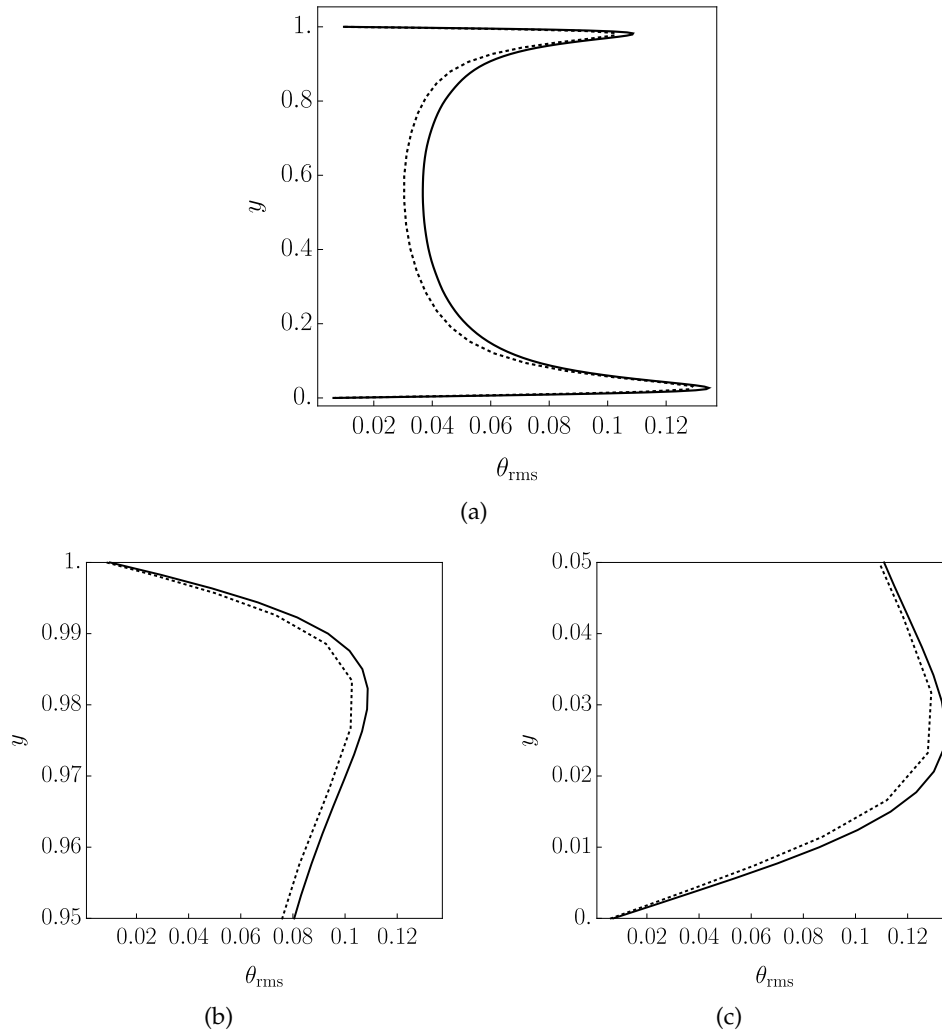


Figure 10. Normalized temperature rms, θ_{rms} , plots of $Ra = 10^7$ at mid-width, $x = 0.5$. (a) across the vertical, (b) zoom on the lower wall and (c) zoom on the upper boundary. The legend is as follows: DNS (—) and LES (.....).

Under non-Oberbeck-Boussinesq conditions, convective transfer is still dominant in the bulk, i.e. $\langle \rho v \theta \rangle_{xzt}$ is practically constant in the bulk. This is confirmed by our DNS data; see figure 3a. However, due to the density fluctuations we have that

$$\langle \rho v \theta \rangle_{xzt} = \langle \rho \rangle_{xzt} \langle \theta' v' \rangle_{xzt} + \langle v \rangle \langle \rho' \theta' \rangle_{xzt} + \langle \rho' v' \theta' \rangle_{xzt} = \text{const} . \quad (3.5)$$

Accordingly, if density fluctuations are significant, this equation implies that $\langle \theta' v' \rangle_{xzt}$ is no longer constant in the bulk as the second and third terms on the right-hand side are nonzero.

In the flow under study, however, the density fluctuations are sufficiently small so as the second and third terms are expected to be negligible. In fact, from post-processing of our DNS data we concluded that this is the case and, furthermore, $\langle \theta' v' \rangle_{xzt}$ is practically constant in the bulk and equal to $\langle \rho v \theta \rangle_{xzt}$.

Therefore, in our case, the observed dip in $\langle \theta' v' \rangle$, shown in figure 11, cannot be attributed to the non-Oberbeck-Boussinesq conditions. We remark however that $\langle \theta' v' \rangle$ is computed at a given x and is time and z averaged only, as opposed to the time and $x - z$ averaged equivalent $\langle \theta' v' \rangle_{xzt}$. In other words, the observed dip of $\langle \theta' v' \rangle$ is not in contradiction with the fact that

$\langle \theta' v' \rangle_{xzt}$ is constant. Moreover, $\langle \theta' v' \rangle$ varies along x ; this is not surprising, as this direction is not homogeneous.

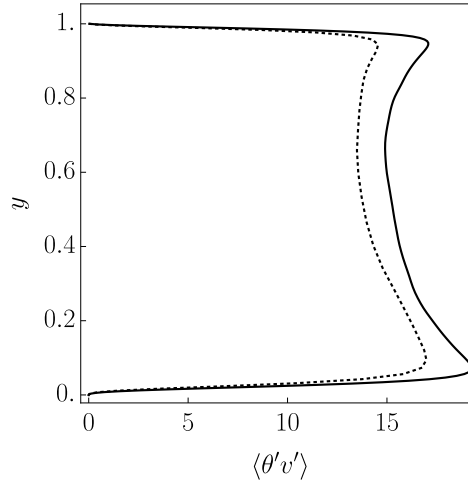


Figure 11. Turbulent heat flux, $\langle \theta' v' \rangle$, plots of $Ra = 10^7$ at mid-width, $x = 0.5$. The velocity has been non-dimensionalised by $\hat{\kappa}/\hat{H}$. The legend is as follows: DNS (—) and LES (⋯⋯).

Also, from figure 11 we see the profile of $\langle \theta' v' \rangle$ predicted by our LES is similar to the one obtained from our DNS data, but the LES results underpredict the values of the turbulent heat flux in the bulk by approximately 10%. Similarly, the peaks near the top and bottom wall are underpredicted by approximately 15%. Overall, we may conclude that the LES predictions of the first and second-order statistics of the flow quantities compare quite satisfactorily with the corresponding DNS data.

(iv) Turbulent kinetic energy budget

In this section we present the TKE budget based on the DNS data. The TKE balance equation is obtained in three steps. First, the momentum equation is multiplied by \mathbf{u} and the average is taken to get an equation for $\mathcal{K} = (1/2)\langle \mathbf{u} \cdot \mathbf{u} \rangle$. Second, the momentum equation is averaged and then multiplied by $\langle \mathbf{u} \rangle$ to give an equation for $\bar{\mathcal{K}} = (1/2)\langle \langle \mathbf{u} \rangle \cdot \langle \mathbf{u} \rangle \rangle$. Finally, subtracting the equation for $\bar{\mathcal{K}}$ from the one for \mathcal{K} yields the sought-after equation for TKE. It is noted that this process removes the term describing the gravitational force from the TKE balance equation. For variable density flows, the process of carrying out the TKE budget is simplified by introducing density-weighted (Favre averaged) quantities. For any given flow quantity ϕ the Favre-averaged equivalent $\{\phi\}$ is defined as

$$\{\phi\} = \frac{\langle \rho \phi \rangle}{\langle \rho \rangle}. \quad (3.6)$$

The mean and fluctuating values are then related by the Favre decomposition,

$$\phi = \{\phi\} + \phi'' . \quad (3.7)$$

The variable k then denotes the turbulent kinetic energy of the density-weighted velocity fluctuations,

$$k = \frac{1}{2} (\mathbf{u}'' \cdot \mathbf{u}'') . \quad (3.8)$$

By following the procedure outlined above, we arrive at the following equation [23,47].

$$\begin{aligned}
\langle \rho \rangle \frac{\partial \{k\}}{\partial t} = & - \underbrace{\nabla \cdot (\langle \rho \rangle \{k\} \{u\})}_{C_k} - \underbrace{\nabla \cdot (\langle \rho \rangle \{k u''\})}_{T_k} - \underbrace{\langle \rho \rangle \{u'' u''\} : \nabla \{u\}}_{P_k} \\
& - \underbrace{\nabla \cdot (\langle p \rangle \{u''\})}_{\Phi_k} - \underbrace{\nabla \cdot (\langle p' u'' \rangle)}_{\phi_k} + \underbrace{\langle p \nabla \cdot u'' \rangle}_{\Pi_k} + \underbrace{\nabla \cdot \langle \tau \cdot u'' \rangle}_{D_k} - \underbrace{\langle \tau : \nabla u'' \rangle}_{\epsilon_k}. \quad (3.9)
\end{aligned}$$

The right-hand-side terms C_k , T_k and P_k represent convection, transport and production of turbulent kinetic energy, respectively. Further, the terms Φ_k and ϕ_k describe, respectively, the work of the mean and fluctuating pressures through fluctuating motions, whereas the term Π_k represents the pressure correlation with the dilatation fluctuation. Finally, D_k describes the viscous diffusion, i.e. the work of viscous stresses through fluctuating motions, and ϵ_k describes the viscous dissipation.

When the flow becomes statistically steady, both sides of equation (3.9) are zero. At the end of our simulation, the computed value of the left-hand side of (3.9) was smaller than 10^{-6} , whereas the sum of the right-hand side was below 20% of the magnitude of the largest term. We therefore consider the flow to be statistically steady. For the purposes of our study we choose to carry out the above budget at mid-height, $y = 0.5$, and mid-width, $x = 0.5$. This analysis provides a global picture of the different contributions of each term in (3.9).

The TKE budget along the horizontal axis at $y = 0.5$ is shown in figure 12 where all terms on the right-hand side of (3.9) are shown, as well as the sum of the RHS terms called, RHS_k . A symmetric profile is observed and we can see that, in the bulk, the mean pressure transport Φ_k is balanced by the viscous dissipation ϵ_k and the fluctuating transport ϕ_k . The term Φ_k is dominant in the core region due to the hydrostatic component $-\{\rho\}|\mathbf{g}|$ of $\nabla\{p\}$, as can be evidenced upon expansion of this term,

$$\Phi_k = \nabla \cdot (\langle p \rangle \langle u'' \rangle) = \langle p \rangle \nabla \cdot \langle u'' \rangle + \langle u'' \rangle \cdot \langle \nabla p \rangle. \quad (3.10)$$

We note that due to the large value of the hydrostatic component of $\nabla\{p\}$, the amplitude of Φ_k is significant. Further, $\langle u'' \rangle$ is quite small (by continuity and due to the fact that the density fluctuations are small), albeit non-zero. Then, this term is multiplied by $\nabla\langle p \rangle$, whose amplitude is large, thereby resulting in a significant value of Φ_k . The contribution of Φ_k is much more pronounced in turbulent natural convection than in channel flows with thermal mixing [23,48]. This is due to the dominance of buoyancy effects in natural convection and exemplifies the different characteristics of turbulence between the two types of flow.

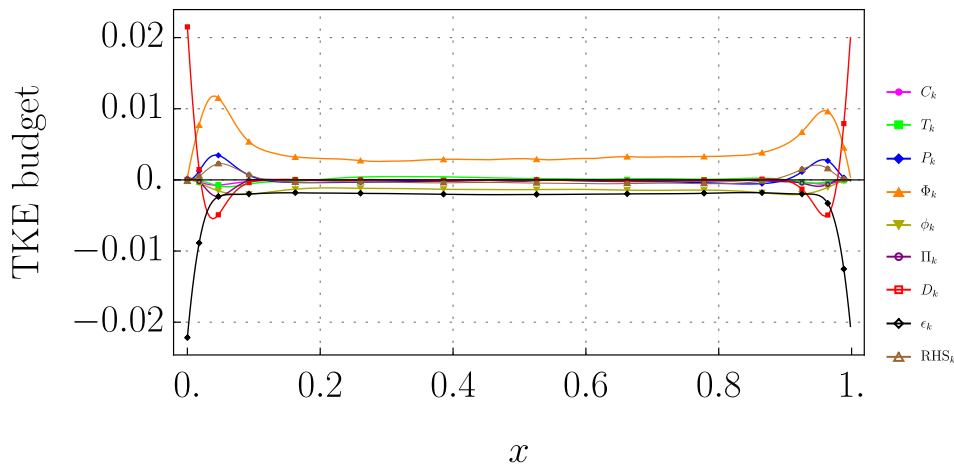


Figure 12. Horizontal TKE budget of DNS at $Ra = 10^7$ at mid-height, $y = 0.5$.

In figure 13 we present a zoom on the side wall. The observed peaks in Φ_k , are predominantly due to the increase in vertical velocity fluctuations $\langle v'' \rangle$ in the near-wall regions. The sum of Φ_k and the production term P_k is then balanced by all remaining terms of opposite sign. In fact, the production term P_k is given as the double interior product between $\langle \rho \rangle \{ \mathbf{u}'' \mathbf{u}'' \}$ and $\nabla \{ \mathbf{u} \}$. Upon expansion, we observed that the important components of P_k in the near-wall regions are those involving $\frac{\partial \{u\}}{\partial y}$ and $\frac{\partial \{v\}}{\partial y}$. Therefore, at these regions it is the velocity gradient in the y direction that contributes the most to the production term. Closer to the walls, all terms go to zero except for D_k and ϵ_k which balanced out one another; this behaviour is also observed in turbulent channel flows with thermal mixing [23] where most of the turbulent kinetic energy is also dissipated at the walls.

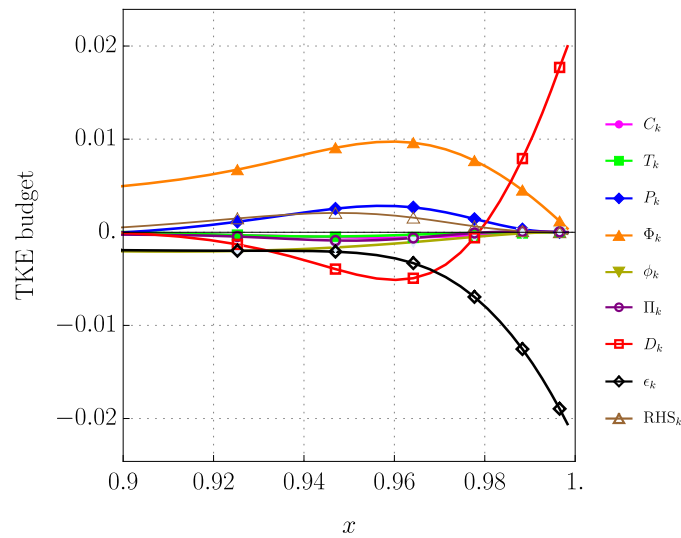


Figure 13. Horizontal TKE budget of DNS at $Ra = 10^7$ at mid-height, $y = 0.5$. Zoom on the right-hand-side wall of figure 12.

The TKE budget along the vertical axis at $x = 0.5$ is given in figure 14, in which the inset shows a zoom on the bulk at $0.4 < y < 0.6$. Unlike the TKE budget across the horizontal axis, an asymmetric profile is observed. However, Φ_k is still the dominant term in the bulk and is balanced predominantly by ϕ_k and the viscous dissipation ϵ_k . In the bulk, the contribution of the other terms to the TKE budget is negligible.

We note that the profile of ϵ_k is flat along the vertical with the exception of the near-boundary regions, this is in-line with the classical experimental observation from Deardroff and Willis [33].

To analyse the behaviour at the boundaries, we present figure 15a for the lower wall and figure 15b for the upper free-slip boundary. At the lower wall boundary layer, Φ_k again increases in magnitude but, unlike in the budget in the horizontal direction, is balanced by the term π_k representing the pressure correlation with the dilatation fluctuation. Closer to the wall, we see again that all terms go to zero except that of diffusion and dissipation. At the upper boundary, unlike at the rigid lower wall, the diffusion and dissipation terms take the same sign and their total is predominately balanced by ϕ_k , the fluctuating pressure transport term.

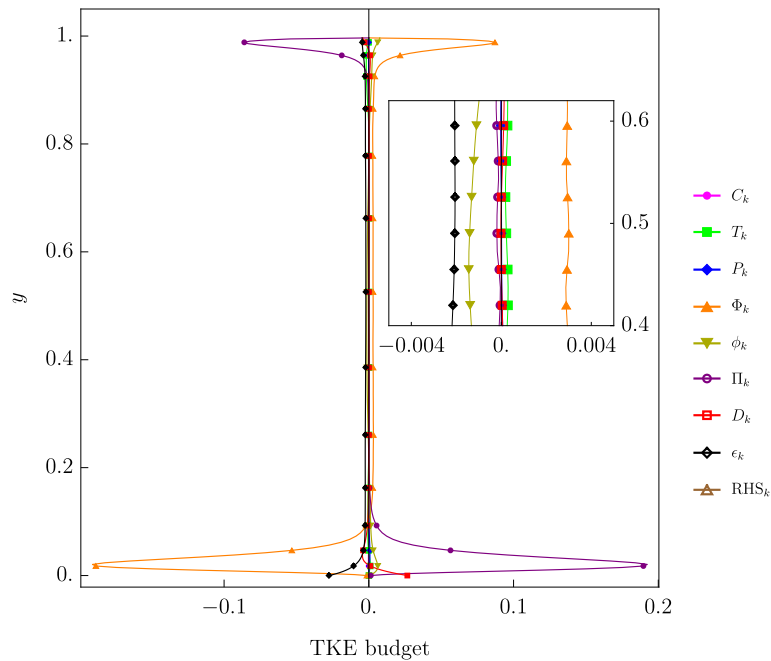


Figure 14. Vertical TKE budget of DNS at $Ra = 10^7$ at $x = 0.5$. The inset is a zoom on the bulk between $0.4 < y < 0.6$.

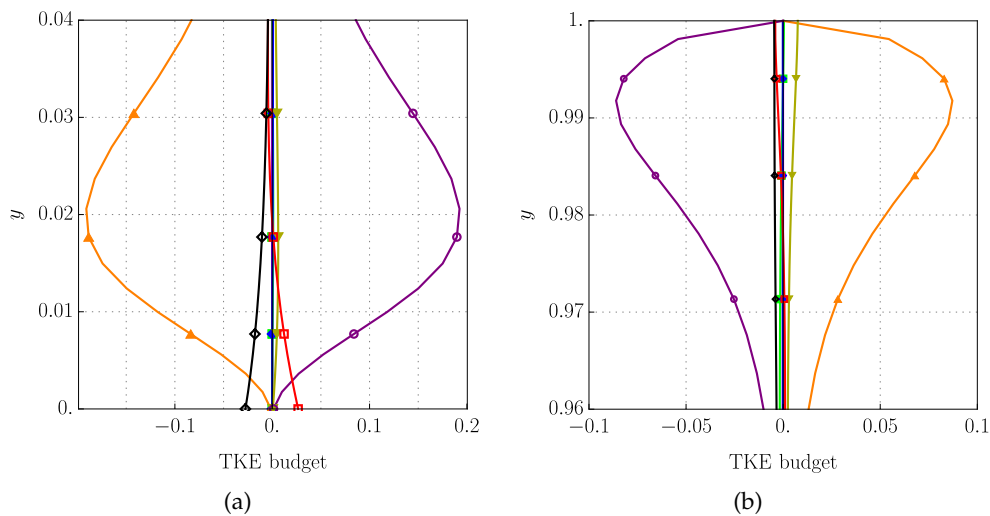


Figure 15. Vertical TKE budget of DNS at $Ra = 10^7$ at $x = 0.5$. (a) zoom on the lower wall and (b) zoom on the upper boundary. The legend is the same as in figure 14.

(b) Analysis of higher-Rayleigh-number flows

We next present and analyze our LES results of the flows at increasing Ra .

(i) Time-averaged flow properties

We first look at the effect of increasing Ra on the heat transfer in the domain. In figure 16 we have plotted the profiles of Nu_y , as well as the profiles of the convective and the diffusive components of Nu . The profiles of Nu_y are flat for all cases except $Ra = 10^9$. The deviation from the flat

profile at $Ra = 10^9$ suggests that averaging over 200 free-fall times may not be fully sufficient for this case. A

Figure 16 also shows the expected trend that increasing Ra will increase Nu . Further, the role of the free-slip upper boundary is to increase Nu in the cavity (see table 6 and [36] for comparison at $Ra = 10^7$) as a result of the fewer hydrodynamic boundary layers. It must be noted, however, that since we have considered only three different Ra , we cannot assess whether soft ($\propto Ra^{\frac{1}{3}}$), hard ($\propto Ra^{\frac{2}{7}}$) or other turbulence scaling would be appropriate. For such an assessment, more simulations with at different Ra are required

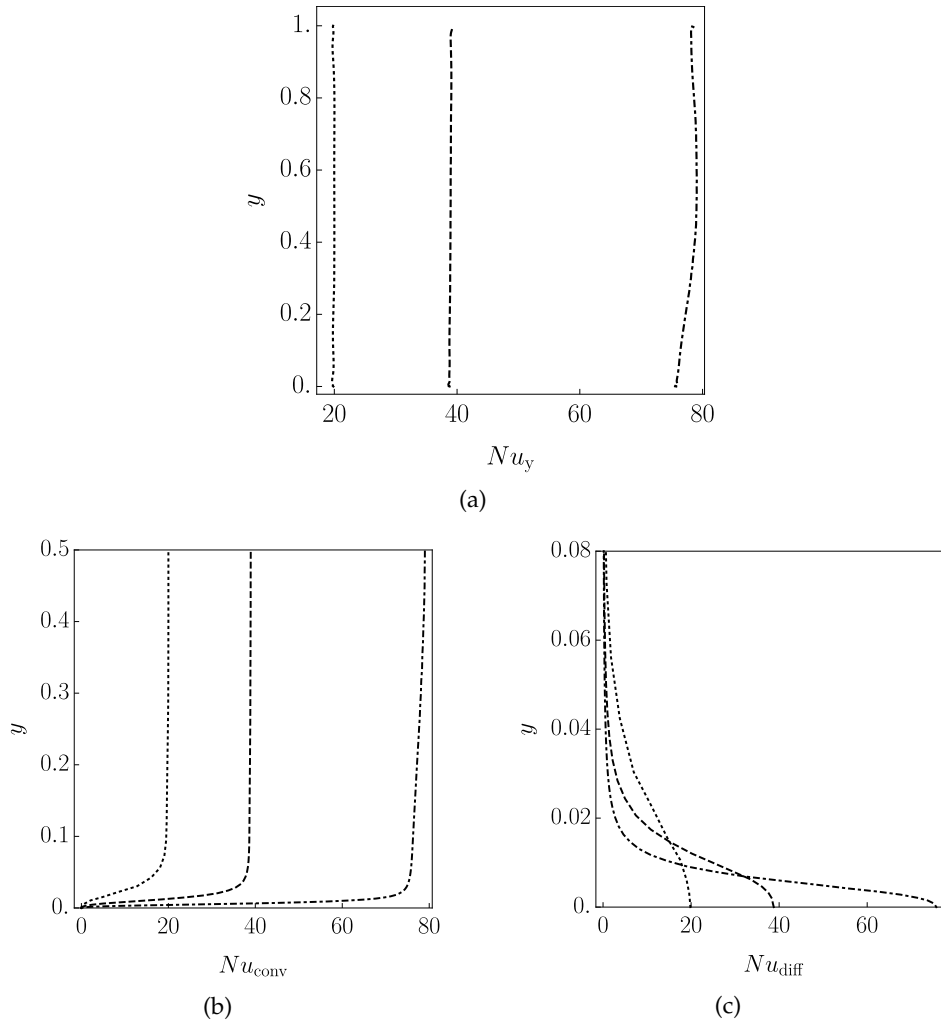


Figure 16. LES plots of the time and area-averaged Nu_y at increasing Ra . (a) Nu_y across the vertical, (b) Nu_{conv} across the lower half of the domain and (c) Nu_{diff} zoom on the lower boundary. The legend is as follows: LES at $Ra = 10^7$ (\cdots), $Ra = 10^8$ ($---$) and $Ra = 10^9$ ($- \cdot -$).

(ii) Flow statistics

In this section we again look at the vertical profiles of the flow but this time assess the effect of increasing Ra . The rms plots of the vertical velocity over increasing Ra are presented in figure 17a where the observed trend is for v_{rms} to increase with Ra , i.e. increasing the turbulence results in stronger vertical velocity fluctuations. We also observe that the parabolic profile persists even at

higher Ra and that the maximum in the bulk is more pronounced at increasing Ra . With respect to the rms plots of the in-plane velocity over increasing Ra we present figure 17b. We can see that the magnitude of the local peak near the lower boundary increases with Ra . The same is true for the turbulent kinetic energy \sqrt{K} , the profile of which is depicted in figure 17c. We conclude that, globally, the rms velocity profiles follow the same trends independently of the Ra ; the only significant difference is the increase in their magnitude with Ra . In other words, we observe a significant increase in the resolved kinetic energy with Ra , as expected.

It is also worth mentioning that the location of the local peak in \bar{u}_{rms} near the lower wall, which signifies the height of the local boundary layer, moves closer to the wall as Ra increases. This is in accordance with the fact that the height of the boundary layer decreases with increasing turbulence intensity.

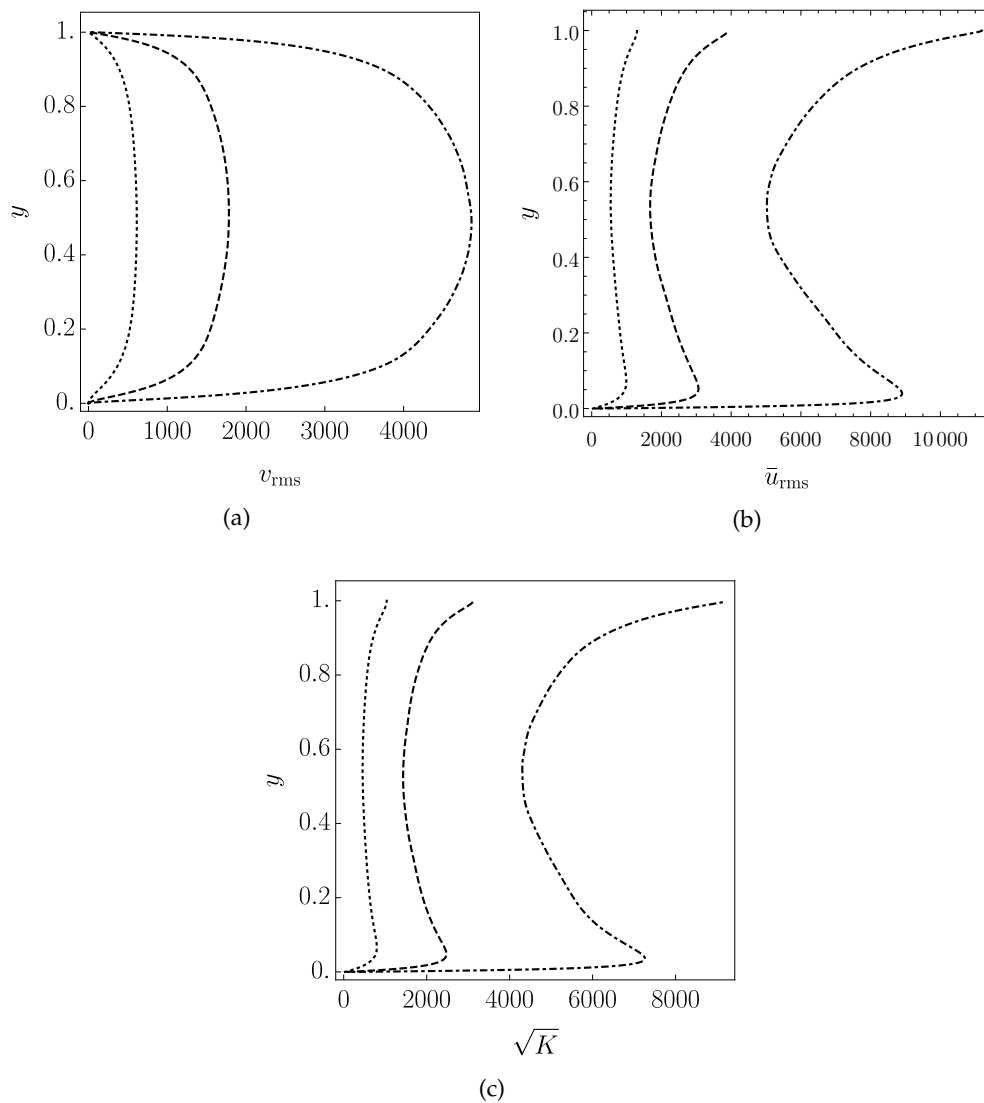


Figure 17. LES plots of velocity rms and turbulent kinetic energy at increasing Ra at mid-width, $x = 0.5$. (a) vertical velocity rms, v_{rms} , (b) in-plane velocity rms \bar{u}_{rms} and (c) square root of the turbulent kinetic energy \sqrt{K} . The velocity has been non-dimensionalised by $\hat{\kappa}/\hat{H}$. The legend is as follows: LES at $Ra = 10^7$ (.....), $Ra = 10^8$ (---) and $Ra = 10^9$ (-.-).

The normalized temperature plots at different Ra are given in figure 18. For the bulk, the same trend is observed in figure 18a as in figure 9a, i.e. $\theta_c < \theta_m$. Increasing Ra has little effect on the magnitude of this shift. However, at the boundaries the observed trend is for the thermal boundary layers to become thinner with increasing Ra . This is quantified by looking at the rms of the normalized temperature.

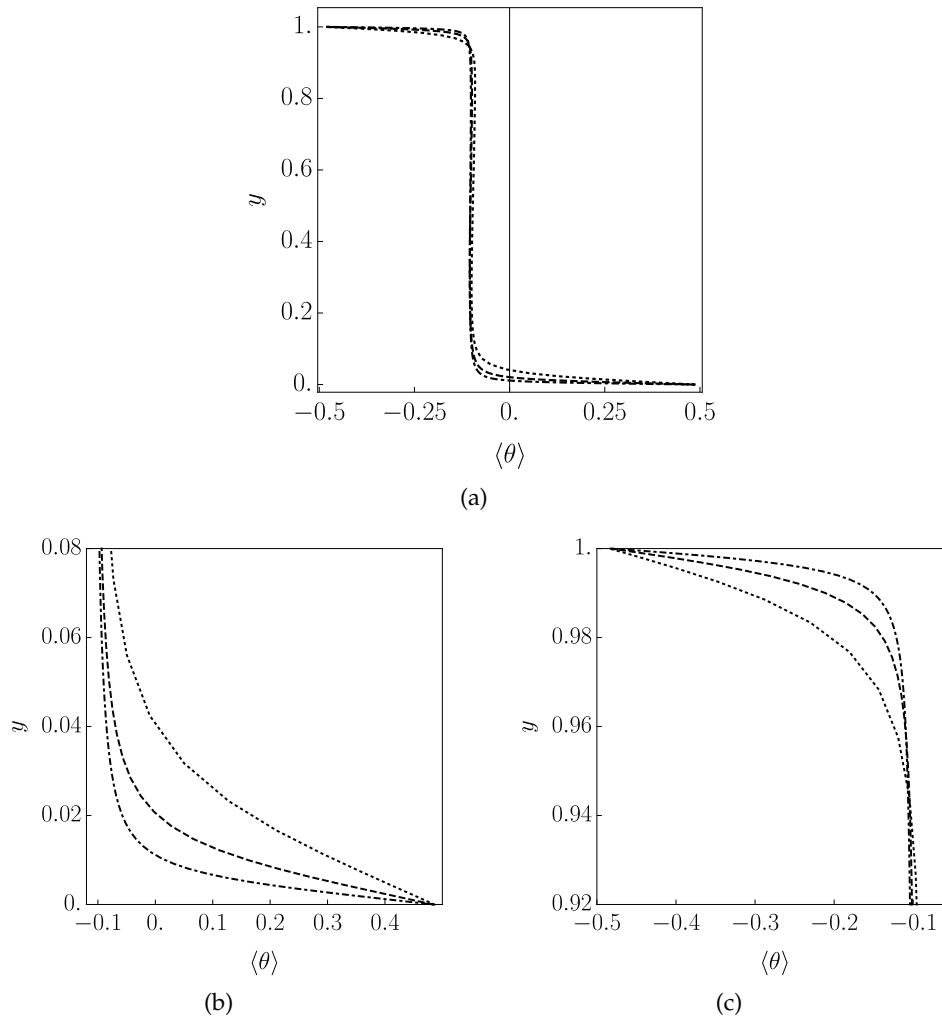


Figure 18. LES plots of mean normalized temperature, $\langle\theta\rangle$, at increasing Ra at mid-width, $x = 0.5$. (a) across the vertical, (b) zoom on the lower wall and (c) zoom on the upper boundary. The legend is as follows: LES at $Ra = 10^7$ (.....), $Ra = 10^8$ (- - -) and $Ra = 10^9$ (- · - ·).

The rms plots of the normalized temperature over increasing Ra are provided in figures 19b and 19c. As Ra is increased, the magnitude of θ_{rms} in the bulk is reduced, i.e. the dip in θ_{rms} becomes more pronounced. A similar trend was observed in [39] over the same range of Ra for classical turbulent RBC. The location of peak temperature variance approaches the boundaries as a result of increasing Ra . This is in accordance with the fact that the thermal boundary layers become thinner with increasing turbulence intensity. The heights of the thermal boundary layers are also provided in table 6. It is noted that at both lower and top boundaries, an increase in Ra appears to *increase* the magnitude of peak in θ_{rms} appears to decrease with Ra . This behaviour is similar to that observed at solid boundaries in classical turbulent RBC.

Table 6. LES refinement, Nu and thermal boundary layer heights.

	Ra	Cells	Nu_y	Nu_G	δ_{uL}	δ_{θ_L}	δ_{θ_U}	$\frac{1}{2Nu}$
DNS	10^7	$110 \times 110 \times 360$	21.4	21.4	0.073	0.027	0.018	0.023
LES	10^7	$40 \times 40 \times 100$	19.9	20.0	0.073	0.031	0.017	0.025
LES	10^8	$80 \times 80 \times 200$	38.9	38.9	0.050	0.015	0.010	0.013
LES	10^9	$130 \times 130 \times 300$	77.5	78.1	0.039	0.007	0.004	0.006

Interestingly in [49], it is postulated whether water-side turbulence conditions, governed by the depth of the water tank in their experiments, could influence evaporation rates. Indeed, experimental results confirmed that increasing water-side Ra for the the same gas-side conditions tend to increase mass transfer at the free surface. It was hypothesized that an increase in θ_{rms} at the interface could be the cause. We note, however, that our LES predictions are not in line with this claim.

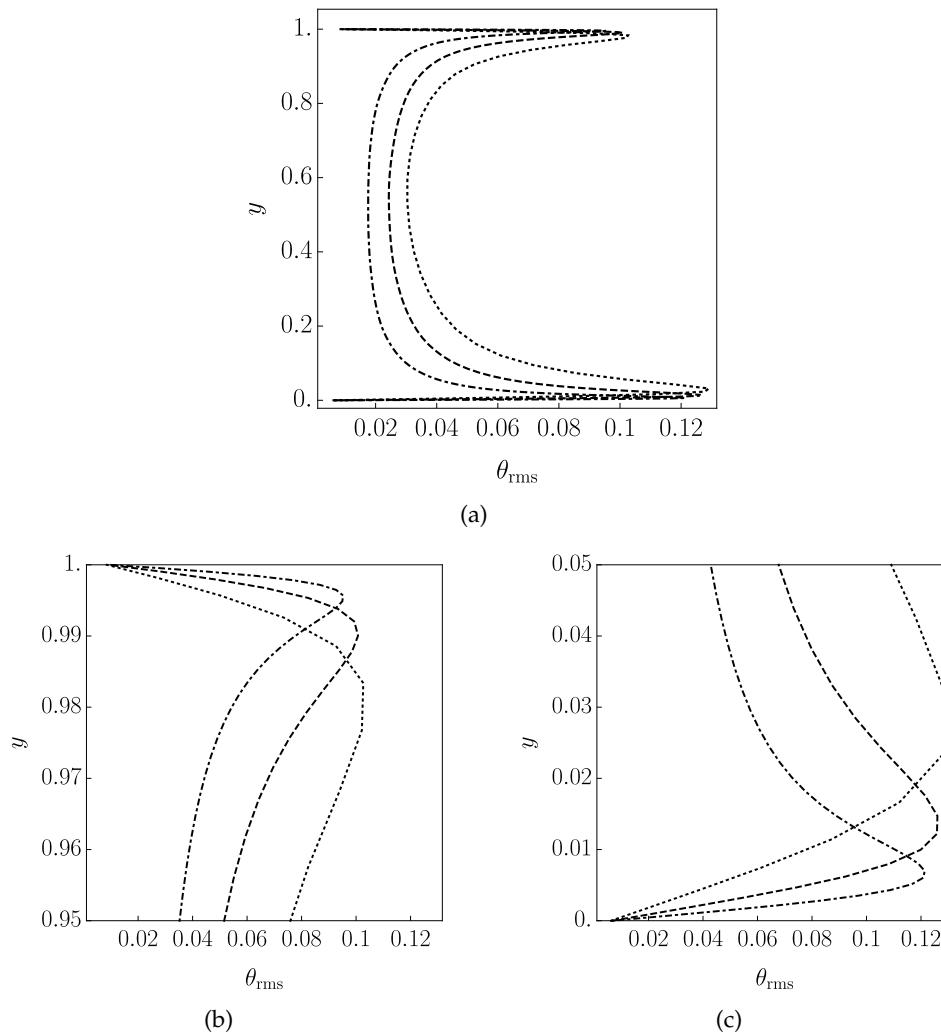


Figure 19. LES plots of normalized temperature rms, θ_{rms} , at increasing Ra at mid-width, $x = 0.5$. (a) across the vertical, (b) zoom on the lower wall and (c) zoom on the upper boundary. The legend is as follows: LES at $Ra = 10^7$ (.....), $Ra = 10^8$ (- - -) and $Ra = 10^9$ (-.-.).

The plots of the turbulent heat flux over increasing Ra are shown in figure 20. As discussed earlier, the profiles are not flat in the core and, moreover, $\langle \theta' v' \rangle$ varies along the inhomogeneous x -direction. The dip in the core is accentuated with Ra , i.e. as the turbulence intensity are increased.

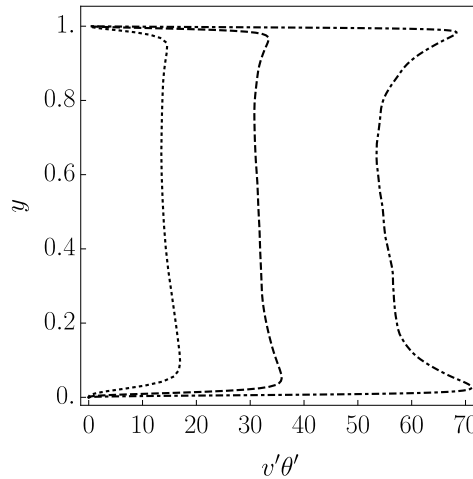


Figure 20. LES plots of turbulent heat flux, $\langle \theta' v' \rangle$, at increasing Ra at mid-width, $x = 0.5$. The velocity has been non-dimensionalised by $\hat{\kappa}/\hat{H}$. The legend is as follows: LES at $Ra = 10^7$ (\cdots), $Ra = 10^8$ ($-\ - -$) and $Ra = 10^9$ ($-\ \cdot - \cdot$).

4. Conclusions

In this article direct numerical and wall-resolved large-eddy simulations of a thermal convective flow have been presented over a range of Ra covering both the soft and hard turbulence regimes. This flow is a simplified version of the thermal convection of water in a cavity heated from below with evaporative heat loss at its free surface. As a first attempt to understand the impact of a free surface on turbulent Rayleigh Bénard Convection, a free-slip upper boundary condition has been implemented. Two important consequences of introducing the free-slip upper boundary are an increase in convective heat transfer (or Nu) as a result of the fewer hydrodynamic boundary layers and the removal of the homogeneity in the thermal boundary layer heights at the lower and upper boundaries.

Another consequence of the free slip at the upper boundary is the asymmetry of the vertical profiles of the first and second-order statistics. As expected, this asymmetry becomes more pronounced with Ra . Further, according to our DNS and LES data, the vertical profiles of $\langle v' \theta' \rangle$ are not flat in the bulk, contrary to that predicted in previous simulations for classical turbulent RBC. Further, according to our simulations, the first and second-order statistics are well produced by the LES when compared to the DNS for the moderate Rayleigh case. However, the LES slightly underpredicts Nu ; this may be, at least partially, attributed to the constant Pr_t presumed in our study.

A turbulent kinetic energy budget was carried out at two locations for the DNS at $Ra = 10^7$; at mid-height and at mid-width. Both profiles showed that, in the bulk, the dominant term was the work of the mean pressure which is balanced by the work of the fluctuating pressure and the turbulent kinetic energy dissipation. Interestingly, the work of the mean pressure is dominant due to the hydrostatic component of the mean-pressure gradient but also depends on the density fluctuations which are small but critically, non-zero. In other words, even though the deviation from the Oberbeck-Boussinesq conditions are small with regard to the fluid density, the effect of this deviation can be significant.

At mid-height, a horizontal TKE profile shows that the equal in magnitude (opposite in sign) terms of TKE diffusion and dissipation terms dominate in the hydrodynamic boundary layers at the vertical side walls; a trend also observed in channel flows. At mid-width, a vertical profile shows the same trend in the hydrodynamic boundary layer at the lower wall. At the free-slip boundary however, all terms approach zero except that of diffusion and dissipation (now of the same sign and different magnitude), their sum being balanced by the fluctuating pressure work term.

Finally, we presented a series of LES at increasing Ra and assessed their first and second-order statistics. The observed trends were as expected, such as the increase in bulk and maximum velocity variance and reduction in thermal boundary layer heights with increasing Rayleigh number. As a next step in our research we intend to implement a variable Pr_t turbulence model and perform further simulations at increased Ra . The idea being to develop a $Nu(Ra)$ scaling for the case in hand and to further quantify the effect on the thermal boundary layer heights beneath the free-slip at the very high Ra flows expected in spent fuel pools.

Data Accessibility. The code, found at www.github.com/WilliamHayOF/lowMachBuoyantPimpleFoam, is publicly available. The code is an extension to the open source C++ code library, OpenFOAM, which can be downloaded from www.openfoam.com.

Authors' Contributions. W.H. adapted the solver from OpenFOAM[®] v1806 for low-Mach number flows, carried out the numerical simulations and participated in the post-processing and analysis of the results. He also participated in the writing of the paper. M.V.P. supervised the code development, participated in the post-processing and analysis of the results and in the writing of the paper. Both authors gave final approval for publication.

Competing Interests. No competing interests.

Funding. The authors gratefully acknowledge the financial support of Bel V, a subsidiary of the Belgian Federal Agency of Nuclear Control.

Acknowledgements. The present research benefited from computational resources made available on the Tier-1 supercomputer of the Fédération Wallonie-Bruxelles, infrastructure funded by the Walloon Region under the grant agreement n°1117545.

References

1. Volino RJ, Smith GB. 1999 Use of simultaneous IR temperature measurements and DPIV to investigate thermal plumes in a thick layer cooled from above. *Exp. Fluids* **27**, 70–78.
2. Flack KA, Saylor JR, Smith GB. 2001 Near surface turbulence for evaporative convection. *Phys. Fluids* **13**, 3338–3345.
3. Saylor JR, Smith GB, Flack KA. 2001 An experimental investigation of the surface temperature field during evaporative convection. *Phys. Fluids* **13**, 428–439.
4. Spangenberg WG, Rowland WR. 1961 Convective Circulation in Water Induced by Evaporative Cooling. *Phys. Fluids* **4**, 743–750.
5. Katsaros KB, Liu WT, Businger JA, Tillman JE. 1976 Heat transport and thermal structure in the interfacial boundary layer measured in an open tank of water in turbulent free convection. *J. Fluid Mech.* **83**, 311–335.
6. Bukhari SJK, Siddiqui MHK. 2006 Turbulent structure beneath air-water interface during natural convection. *Phys. Fluids* **18**, 035106.
7. Kerr RM. 1996 Rayleigh number scaling in numerical convection. *J. Fluid Mech.* **310**, 139–179.
8. Shishkina O, Wagner C. 2007 Local heat fluxes in turbulent Rayleigh-Bénard convection. *Phys. Fluids* **19**, 085107.
9. Verzicco R, Camussi R. 2003 Numerical experiments on strongly turbulent thermal convection in a slender cylindrical cell. *J. Fluid Mech.* **477**, 19–49.
10. Amati G, Koal K, Massaioli F, Sreenivasan KR, Verzicco R. 2005 Turbulent thermal convection at high Rayleigh numbers for a Boussinesq fluid of constant Prandtl number. *Phys. Fluids* **17**, 121701.
11. Stevens R, Verzicco R, Lohse D. 2010 Radial boundary layer structure and Nusselt number in

- Rayleigh-Bénard convection. *J. Fluid Mech.* **643**, 495–507.
12. Benard H. 1900 Les tourbillons cellulaires dans une nappe liquide. *Rev. Gén. Sciences Pure Appl.* **11**, 1261–1271.
 13. Ahlers G, Grossman S, Lohse D. 2009 Heat transfer and large scale dynamics in turbulent Rayleigh-Bénard convection. *Rev. Mod. Phys.* **81**, 503–537.
 14. Siggia ED. 1994 High Rayleigh number convection. *Annu. Rev. Fluid Mech.* **26**, 137–168.
 15. Lohse D, Xia K. 2010 Small-Scale Properties of Turbulent Rayleigh-Bénard Convection. *Annu. Rev. Fluid Mech.* **42**, 335–364.
 16. Zikanov O, Slinn DN, Dhanak MR. 2002 Turbulent convection driven by surface cooling in shallow water. *J. Fluid Mech.* **464**, 81–111.
 17. Gray DD, Giorgini A. 1976 The validity of the Boussinesq approximation for liquids and gases. *Int. J. Heat Mass Tran* **19**, 545–551.
 18. Bückle U, Perić M. 1992 Numerical simulation of buoyant and thermocapillary convection in a square cavity. *Numer. Heat. Tr. A.* **21**, 121–141.
 19. Ahlers G, Fontenele Araujo F, Funfschilling D, Grossmann S, Lohse D. 2006 Non-Oberbeck-Boussinesq effects in strongly turbulent Rayleigh-Bénard convection. *J. Fluid Mech.* **569**, 409–445.
 20. National Academies of Sciences, Engineering and Medicine. 2016 *Lessons Learned from the Fukushima Nuclear Accident for Improving Safety and Security of U.S. Nuclear Plants: Phase 2*. The National Academies Press.
 21. Majda A, Sethian J. 1985 The derivation and numerical solution of the equations for zero-Mach number combustion. *Combust. Sci. Technol.* **42**, 185–205.
 22. Lessani B, Papalexandris MV. 2006 Time accurate calculation of variable density flows with strong temperature gradients and combustion. *J. Comput. Phys.* **212**, 218–246.
 23. Georgiou M, Papalexandris MV. 2018 Direct numerical simulation of turbulent heat transfer in a T-junction. *J. Fluid Mech.* **845**, 581–614.
 24. Papalexandris MV. 2019 On the applicability of Stokes' hypothesis to low-Mach-number flows. *Continuum Mech. Therm.* doi: 10.1007/s00161-019-00785-z.
 25. Wagner W, Kretschmar HJ. 2008 *International Steam Tables Properties of Water and Steam Based on the Industrial Formulation IAPWS IF97*. Springer.
 26. Kaczorowski M, Wagner C. 2008 Analysis of the thermal plumes in turbulent Rayleigh-Bénard convection based on well-resolved numerical simulations. *J. Fluid Mech.* **618**, 89–112.
 27. Rhie CM, Chow WL. 1983 Numerical Study of the Turbulent Flow Past an Airfoil with Trailing Edge Separation. *AIAA* **21**, 1525–1532.
 28. Weller HG, Tabor G, Jasak H, Fureby C. 1998 A tensorial approach to computational continuum mechanics using object-oriented techniques. *Comput. Phys.* **12**, 620–631.
 29. Issa RI. 1985 Solution of the Implicitly Discretized Fluid Flow Equations by Operator-Splitting. *J. Comp. Phys.* **62**, 40–65.
 30. Oliviera PJ, Issa RI. 2001 An improved PISO algorithm for the computation of buoyancy driven flows. *Numer. Heat Tr. B-Fund* **40**, 473–493.
 31. Hassanaly M, Koo H, Lietz CF, Chong ST, Raman V. 2018 A minimally-dissipative low-Mach number solver for complex reacting flows in OpenFOAM. *Comput. Fluids* **162**, 11–25.
 32. Grötzbach G. 1983 Spatial Resolution Requirements for Direct Numerical Simulation of the Rayleigh-Bénard convection. *J. Comput. Phys.* **49**, 241–264.
 33. Deardorff JW, Willis GE. 1967 Investigation of turbulent thermal convection between horizontal plates. *J. Fluid Mech.* **28**, 675–704.
 34. Niemala JJ, Skrbek L, Sreenivasan KR, Donnelly RJ. 2000 Turbulent convection at very high Rayleigh numbers. *Nature* **404**, 837–840.
 35. Heslot F, Castaing B, Libchaber A. 1987 Transitions to turbulence in helium gas. *Phys. Rev. A* **36**, 5870–5873.
 36. Kaczorowski M, Xia K. 2013 Turbulent flow in the bulk of Rayleigh-Bénard convection: small-scale properties in a cubic cell. *J. Fluid Mech.* **722**, 596–617.
 37. Shishkina O, Stevens R, Grossman S, Lohse D. 2010 Boundary layer structure in turbulent thermal convection and its consequences for the required numerical resolution. *New J. Phys.* **12**, 075022.
 38. Tennekes H, Lumley JL. 1972 *A first course in turbulence*. The MIT Press.
 39. Peng SH, Hanjalic K, Davidson L. 2006 Large-eddy simulation and deduced scaling analysis of Rayleigh-Bénard convection up to $Ra = 10^9$. *J. Turbul.* **7**, N66.

40. Meneveau C, Lund TS, H. CW. 1996 A Lagrangian dynamic subgrid-scale model of turbulence. *J. Fluid Mech.* **319**, 353–385.
41. Lessani B, Papalexandris MV. 2008 Numerical study of turbulent channel flow with strong temperature gradients. *Int. J. Numer. Method. H* **18**, 545–556.
42. Davidson L. 2009 Large Eddy Simulations: How to evaluate resolution. *Int. J. Heat Fluid Fl.* **30**, 1016–1025.
43. Kimmel SJ, Domaradzki JA. 2000 Large eddy simulations of Rayleigh-Bénard convection using subgrid scale estimation model. *Phys. Fluids* **12**, 169–184.
44. Foroozani N, Niemala JJ, Armenio V, Sreenivasan KR. 2014 Influence of container shape on scaling of turbulent fluctuations in convection. *Phys. Rev. E* **90**, 063003.
45. Belmonte A, Tilgner A, Libchaber A. 1994 Temperature and velocity boundary layers in turbulent convection. *Phys. Rev. E* **50**, 269–279.
46. Peng SH, Hanjalic K, Davidson L. 2005 Numerical analysis of Rayleigh-Bénard convection using Large Eddy Simulations at High Rayleigh Numbers. *Proc. 4th Int. Symp. on Turbulence and Shear Flow Phenomena* **3**, 983–988.
47. Chaissang P, Antonia RA, Anselmet F, Joly L. 2002 *Variable Density Fluid Turbulence*. Springer Science+Business Media Dordrecht.
48. Georgiou M, Papalexandris MV. 2017 Turbulent mixing in T-junctions: The role of the temperature as an active scalar. *Int. J. Heat Mass Tran.* **115**, 793–809.
49. Bower SM, Saylor JR. 2009 A Study of the Sherwood-Rayleigh relation for water undergoing natural convection-driven evaporation. *Int. J. Heat Mass Tran.* **52**, 3055–3063.